Real-Time Tracking of Tumor Invasion Dynamics in Organotypic Brain Slices at Subcellular Resolution

Jana B. Petr[1], Meng-Syuan Lin[2], Dina Hochuli[2], Andreas Hierlemann[1], Martin Baumgartner[2*], Mario M. Modena[1*]

[1]ETH Zurich, Department of Biosystems Science and Engineering, Basel, Switzerland
[2]University Children's Hospital, Children's Research Centre, Division of Oncology, Zurich, Switzerland
**Corresponding authors: Martin.Baumgartner@kispi.uzh.ch, mario.modena@bsse.ethz.ch*

Abstract

Understanding how tumor cells invade and interact with their microenvironment is crucial for advancing cancer treatment strategies. However, replicating *in vitro* the heterogeneity and cytoarchitecture of organs, particularly of the brain, remains highly challenging. Here, we developed a tumor / brain slice co-culture model to investigate how medulloblastoma cancer cells invade the cerebellar microenvironment. To monitor invasion in real time, we devised PHIROS, a microfluidic Platform for High-Resolution Imaging of Organotypic Slices. PHIROS enables the aseptic culturing of organotypic slices and long-term, high-resolution imaging of invading tumor cells in cerebellar slices. Tissue health could be maintained over multiple days by controlled perfusion with oxygenated medium in a closed environment, and tissue functionality was confirmed through spontaneous astrocytic calcium signals during perfusion culturing. We utilized PHIROS to observe actin cytoskeleton reorganization and the dynamic localization of the immune-checkpoint marker B7-H3 during cancer invasion, and to see how cancer cells responded to and remodeled their microenvironment. PHIROS provided novel insights into medulloblastoma cell invasion in a physiologically relevant model with the potential to unlock new therapeutic strategies.

Main

Disease mechanisms are complex phenomena, involving the interplay of pathological cells with a multitude of healthy cell types in the microenvironment. However, in *in vitro* assays, microenvironment interactions are typically investigated by culturing a small sub-set of selected cell types on a plastic substrate, which minimizes heterogeneous cell-cell interactions and constitutes a simplified test environment. Although this approach provides a controlled and reproducible test environment, it often lacks physiological relevance[1,2]. The lack of heterogenous cell-cell contacts is particularly limiting for investigating diseases of the central nervous system (CNS), where maintaining the integrity of neuronal connectivity and tissue architecture is essential for replicating physiological functions[3,4]. This aspect is of great importance for studying brain tumors, where cell heterogeneity and connectivity play crucial roles in determining disease progression[5-8]. To advance our understanding of the driving mechanisms behind tumor formation and progression, models that closely recapitulate the complexity of *in vivo* tissue environments are needed. Complex 3D models of brain diseases have been presented in literature, including spheroid[9,10] and organoid[11,12] models, which, albeit providing advantages over traditional 2D models, often lack the native extracellular matrix in which cells interact and feature poor brain organization[13] as well as large heterogeneity in cellular organization[14-16]. Acute or organotypic tissue slices, which feature a physiologically relevant tissue environment with preserved functional connectivity and cytoarchitecture, represent an alternative model system for fundamental and translational *in vitro* research[17,18]. Tissue slices preserve the heterogeneity, connectivity, and functionality of the original tissue, which renders them an attractive model for neurooncological research[17,19-21]. In particular, organotypic tissue slices, which largely preserve an intact and organized cytoarchitecture, are

valuable models for studying the effects of the tumor microenvironment (TME). By engrafting tumor cells on healthy organotypic slices, tumor-host tissue interactions can be investigated in a controlled and accessible environment over multiple days[22,23]. Understanding the interactions between tumor, glial and neuronal cells is critical, as the interplay has direct and indirect effects on tumor initiation [24], progression [25], and metastasis [26]. Co-culture models using murine brain slices in combination with human-derived brain tumor cells are increasingly used for fundamental research[27,28] and compound testing[29-31].

To preserve tissue viability during ex vivo culturing, brain slices are maintained either on a porous membrane at an air-liquid interface (ALI)[19] or alternatingly exposed to medium and air[32]. Consequently, these culturing methods prohibit continuous optical access to the sample to monitor dynamic processes in real-time and over multiple days, limiting possible readouts to endpoint analysis or only a few hours of continuous monitoring.

To address this limitation and enable the investigation of long-term cellular events, such as tumor invasion, we have developed a microfluidics-based platform enabling real-time confocal microscopy. The platform allows for investigation of tumor invasion and cell-cell interaction in a tissue context for multiple days under aseptic conditions, while preserving brain-tissue viability and functionality. The microfluidic setup allows for precise control of environmental parameters, such as oxygen concentration in the medium and medium replenishing rate. We first investigated tissue functionality by monitoring calcium dynamics in astrocyte populations in murine cerebellar slices using genetically encoded calcium indicators. We then engrafted cells of medulloblastoma, the most common malignant brain tumors in children[33], on the slices and monitored tumor cell motility and interactions within the cerebellar microenvironment.

Results and Discussion

Platform for long-term high-resolution imaging of organotypic brain slices

To overcome the limitations of current culturing methods for *ex vivo* slices and to enable long-term investigations of dynamic processes at subcellular resolution, we developed PHIROS (**P**latform for **Hi**gh-**R**esolution Imaging of **O**rganotypic **S**lices). PHIROS enables (i) static culturing at the air-liquid interface (ALI) to support tissue reorganization and recovery after slicing, (ii) perfused culturing in a closed environment to perform continuous, long-term high-resolution imaging under aseptic conditions, and (iii) subsequent tissue fixation and recovery for downstream analysis. Once placed on the platform, the brain slices do not require any further handling during culturing and for imaging, which prevents tissue damage resulting from transferring slices to different substrates.

The platform consists of four main parts (**Figure 1A** and **Supplementary 1A-B)**: i) a polymethylmethacrylate (PMMA)-based slice holder of 22.5 mm diameter, featuring a microfluidic channel for perfusion culturing in a closed environment; ii) a hydrophilic polytetrafluoroethylene (PTFE) membrane with a pore size of 0.4 µm, bonded to the slice holder, to enable static culturing during tissue recovery; the assembly of i) and ii) is further referred to as the “culture chip”; iii) a PMMA-based support part; iv) an adhesive foil for sealing the assembly to enable perfusion. To perform static culturing, the culture chip is placed on a commercially available tissue-culture insert. The medium of the slices on the culture chip is changed by transferring the whole tissue-culture insert into a new well with fresh medium, which corresponds to the established procedure for culturing tissue slices.

In our experiments, we cultured cerebellar slices of murine origin for 14-18 days after tissue resection at the ALI to enable tissue recovery and Purkinje cell layer reorganization. We also used the static recovery period for further experimental interventions, such as the labeling of specific cell subpopulations by using adeno-associated-virus (AAV) vectors. After tissue

reorganization, we placed medulloblastoma spheroids onto the tissue slices and let the cells invade the tissue for 72 h under static culturing conditions before we sealed the slice compartment with a transparent polystyrene foil and began the imaging. The sealing was carried out under sterile conditions to preserve an aseptic culturing environment. The platform was then transferred to the holder and placed onto the stage of a spinning-disk confocal microscope. Up to 3 chips, accommodating a total of 6 to 9 cerebellar slices, were perfused and imaged in parallel **(Supplementary 1C**). To support brain-slice viability in the closed microfluidic chamber, the medium was oxygenated using a custom-made gas exchanger. A dissolved oxygen concentration of ~30 mg/L was found sufficient to support tissue health while preventing bubble formation in the tubing. The medium was transferred from the medium reservoir through the gas exchanger to the platform using a peristaltic pump (**Figure 1B, Supplementary 2**). 70% of the medium in the chamber was exchanged every hour to avoid nutrient and oxygen depletion, and the accumulation of cellular metabolites in the small microfluidic chamber. Thus, by enabling both static and perfusion culturing in a closed chamber, PHIROS enables the monitoring of dynamic processes at tissue and single-cell levels during several days using confocal microscopy (**Figure 1C**).

Organotypic cerebellar slices cultured on chip retained cytoarchitecture

We first confirmed that static culturing at an ALI on two superimposed porous membranes does not impede the reorganization of cerebellar slices. Murine cerebellar slices from P10-P12 mice were cultured either on tissue-culture inserts only or on the culture chip placed on a tissue-culture insert, and the reorganization[34] of the slices was compared after 14 days of *in vitro* (DIV14) culturing (**Figure 2A**). For both scenarios, slices appeared transparent, which is an indication of good tissue health and maturation[17] (**Supplementary 3**). Immunofluorescence (IF) staining revealed a continuous Purkinje cell layer along the tissue convolutions, a dense granule cell population, and astrocyte networks in the slice (**Figure 2B-D, Extended Data 1**). Importantly, the Purkinje cell layer was flanked by well-organized granule and molecular layers, indicating a physiologically relevant reorganization of the tissue slice during the static culturing period.

During chip development, we quantified key properties of the Purkinje cells, namely cell density and cell size, as these parameters provided clear indicators of tissue viability. We tested different designs and membrane materials for the chip fabrication. Non-optimal culturing conditions resulted in sparse Purkinje cell layers featuring large cell somas, disorganized Purkinje cells, or strongly disrupted Purkinje cell layers (**Supplementary 4**). In the final chip version, the Calbindin staining revealed a mean Purkinje cell soma area of 2028 μm^3 and a cell density of 0.0014 cells/μm^2, which were in good accordance with values measured in cerebellar slices cultured on tissue-culture inserts, and with previously reported values for Purkinje cell density *in vivo*[35] (**Figure 2E-F**). The obtained values confirmed that chip geometry and culturing on two superimposed membranes did not affect tissue viability during static culture and enabled the reorganization of the cellular layers in organotypic cerebellar slices.

Oxygenated perfusion culture supported tissue viability during long-term imaging

We then sought to determine whether the culturing of cerebellar organotypic slices in a closed microfluidic channel under perfusion conditions affected tissue viability. After the ALI culture, the culture chips were removed from the tissue-culture inserts and sealed under aseptic conditions. The closed assemblies were placed on the microscope stage inside an environmental control box to maintain 37˚C during imaging (**Figure 3A**). As the flow of the oxygenated medium may disrupt endogenously established chemical gradients due to wash-out of released soluble factors, we decided to minimize the perfusion in the system for long-term imaging by introducing a pulsatile flow protocol with hourly partial medium exchanges, followed by one hour of no flow. This perfusion strategy resulted in a daily medium consumption of ~1.4 mL, a volume comparable to standard culturing conditions. We assessed cell viability

137 under perfusion using a cleaved caspase-3/7 live-cell stain to visualize apoptotic cells in real-
138 time during long-term perfusion culturing. Cell viability was assessed at the start of the
139 perfusion (day 1), after 24 (day 2) and 48 h (day 3). As a positive control, the slices were
140 treated with 40 µM doxorubicin after 48 h of perfusion culture to induce apoptosis in the tissue
141 slices (**Figure 3B, Extended Data 2A .**). The low number of caspase-3/7-positive cells prior to
142 doxorubicin exposure indicated good tissue health in the sealed microfluidic chip throughout
143 the 48 h of perfusion. No significant increase in apoptotic cells was observed during the
144 perfusion period, which further confirmed that medium oxygenation and pulsatile perfusion
145 supported cell viability. However, the metabolic oxygen consumption of the tissue in a small
146 chamber volume during the no-flow periods may induce hypoxic stress. We therefore looked
147 at the expression of the hypoxia transcription factor HIF1-α in the tissue slices by
148 immunofluorescent analysis. We compared the cerebellar slices cultured using the pulsatile
149 flow protocol perfusion with slices either cultured at the ALI or submerged for 24 or 48 hours
150 under 2 ml of medium, to mimic the conditions of continuous, long-term imaging using
151 immersion objectives. Nuclear localization of HIF1-alpha, indicative of hypoxia, was quantified
152 and normalized against control ALI conditions. Submerged, statically cultured slices showed a
153 16.8- and 18.8-fold increase in hypoxia levels after 24 and 48 hours, respectively, while
154 pulsatile perfusion with oxygenated medium resulted in a 4.2-fold increase with respect to the
155 ALI control condition (**Figure 3D, Extended Data 2B**). While the results show that pulsatile
156 perfusion may induce some hypoxic stress in comparison to culturing at the ALI, the stress
157 was substantially lower than that in submerged static slice cultures, indicating that medium
158 oxygenation in combination with stop-flow perfusion supported tissue health in the closed
159 microfluidic chamber.

160 **Ca^{2+} imaging in cerebellar astrocytes confirms tissue functionality**

161 To verify the functional viability of the cerebellar slices, we examined spontaneous astrocyte
162 dynamics after tissue reorganization. Astrocytes exhibit complex intracellular calcium Ca^{2+}
163 signaling dynamics that can be effectively monitored using genetically encoded calcium
164 indicators[36,37]. Astrocytes represent a key component of the brain TME, as tumor cells can
165 integrate into astrocytic networks[38], and astrocytes actively contribute to medulloblastoma
166 progression through the secretion of cytokines and TME remodeling[25,39].

167 Cerebellar slices from P8-P10 mice were transduced with AAV-hGFAP-GCaMP6f at DIV4 and
168 DIV 6 during static culturing to express the genetically encoded Ca^{2+} sensor GCaMP6f in the
169 astrocytic population. The slices were then cultured at the ALI for 10 days to enable consistent
170 sensor expression (**Figure 4A***)*. As GCaMP6 imaging is carried out in serum and phenol-red
171 free media, we transiently replaced the culture medium by artificial cerebrospinal fluid (aCSF)
172 for the duration of the Ca^{2+} imaging using the flow system. Between the imaging sessions,
173 standard culture medium conditions were reinstalled to support tissue viability. PHIROS
174 allowed the continuous monitoring of the same region of interest (ROI) over three days, which
175 enabled capturing of intracellular Ca^{2+} dynamics of the same astrocytes over consecutive days
176 (**Figure 4B-D**, **Supplementary Video 1**).

177 We detected intracellular Ca^{2+} signal fluctuations with consistent intensity changes (~0.2 ΔF/F)
178 in astrocytic processes across the three days (**Figure 4E**). The analysis of Ca^{2+} event
179 characteristics using the AQuA2 software[40] revealed consistent patterns in event duration,
180 area, and intensity throughout the 3 days long perfusion culture (**Figure 4F, Extended Data**
181 **3**).

182 Next, we investigated the difference in Ca^{2+} events between velate astrocytes and Bergmann
183 glia cells. These two specialized cerebellar astrocytes have distinct morphologies, molecular
184 signatures and local connections to different neurons[41], allowing us to distinguish the two cell
185 types during imaging. Bergmann glia cells extend radial processes across the Purkinje cell

186 layer to the pial surface, while velate astrocytes are scattered within the granule cell layer[42].
187 Our results showed that Ca^{2+} fluctuations occurred in the cell body as well as at processes in
188 both astrocyte subtypes. Additionally, we observed Ca^{2+} waves spreading within local astrocyte
189 networks (**Figure 4G-H, Supplementary Video 2**). A comparison of area, duration and
190 fluorescence intensity of the observed calcium events revealed that the area of most calcium
191 events for both Bergmann glia and velate astrocytes fell in the 2.3-250 μm^2 range, while the
192 duration spanned from 1.6 to 60 s (**Figure 4 G/H**), indicating no difference in intracellular Ca^{2+}
193 fluctuations between Bergmann glia cells and velate astrocytes.

194 **Actin cytoskeleton dynamics and tissue-invasive behavior of medulloblastoma cells**

195 An unresolved question in the field is how tumor cells dynamically interact with the TME. To
196 address this, we used PHIROS for real-time observation of medulloblastoma (MB) invasion in
197 the tissue slices. Analogous to the workflow for Ca^{2+} imaging, the static culturing period was
198 used to specifically label astrocytes by AAV transduction of hGFAP-driven mCherry enabling
199 the visualization of the astrocyte soma and processes. We used the highly invasive ONS-76
200 medulloblastoma (MB) cell line expressing lifeact-enhanced green fluorescent protein (LA-
201 eGFP) to track the dynamics of the F-actin cytoskeleton of the tumor cells. The ONS-76-LA-
202 eGFP cells, a model of SHH-activated MB, were seeded in a ultra-low attachment plate to form
203 spheroids of ~2500 cells, which were then placed on the cerebellar slices 72 h prior to the start
204 of the imaging assay (between DIV 16 and 19). Pre-incubation in static conditions enabled the
205 tumor cells to engraft and invade the tissue. Following this static invasion period, the chips
206 were sealed, connected to the fluidic system on the confocal microscope, and the 48 h imaging
207 was started (**Figure 5A**).
208 Notably, the tumor cells stopped exploring the cerebellar tissue microenvironment under
209 continuous perfusion, possibly because the flow interfered with the establishment or
210 maintenance of the chemical gradient. This observation revealed the potential relevance of
211 TME chemical gradient sensing for tissue invasion. To limit the removal of chemical gradients,
212 we introduced a pulsatile flow protocol where ~70% of the medium in the culture chip was
213 exchanged over 7 minutes every hour, while image acquisitions were performed outside the
214 flow intervals.
215 We observed different types of cell behavior and phenotypes, which we assigned to four
216 different clusters (**Figure 5B, Extended Data 4A**): i) Highly explorative, but low invasive cells
217 at the MB spheroid edge; ii) TME-reorganizing, motile cells at the spheroid edge; iii) motile, but
218 non-invasive cells in the center of the spheroid mass; iv) highly explorative and invasive cells
219 at the invading front. The trajectories of single cells obtained by tracking analyses revealed
220 large cell displacements in clusters *ii* and *iv.* Cells in cluster *ii* exhibited rapid morphological
221 changes, featuring high morphological plasticity and motility, but little net displacement,
222 whereas cells in cluster *i* remained largely stationary despite high F-actin dynamics (**Figure**
223 **5C, Supplementary Video 3**). Interestingly, cells in cluster *i* were often surrounded by a
224 pronounced network of mCherry-positive astrocytes, which may affect the motility of these
225 tumor cells. Additionally, the tumor cells were often inter-connected via actin rich, transient thin
226 bridges, forming a loose network of connected cells (**Extended Data 4A, Extended Data 5**),
227 reminiscent of tumor microtubes, a feature that has been reported for different types of invasive
228 tumors[43,44]. We also observed high F-actin dynamics in cluster *iii* cells. However, cells in this
229 cluster could not be tracked as single cells due to the high signal density, which masked cell
230 movements between observation intervals.
231 To more broadly assess cell dynamics in cluster *iii* and across the whole slice, we performed
232 particle velocimetry analysis (**Figure 5D, Supplementary 6**). We computed and plotted the
233 mean magnitude velocity and the standard deviation of the velocity (STDV) to reveal cell
234 velocity fluctuations. The highest velocities were recorded in cluster *ii,* consistent with our
235 single cell tracking data. The high STDVs in cluster *iii* are representative of dynamic cell
236 behaviors. Differences in the chemical and mechanical cues of the cerebellar slices near these

cells may explain their reduced invasiveness compared to cluster *iv* cells. Cluster *ii* cells actively reorganized the TME of the cerebellar slices, using actin-rich structures to exert forces on mCherry-positive astrocytes, which is also reflected in the observed local velocity patterns (**Figure 5D**). Cluster *iii* cells typically followed the invasive front cells belonging to cluster *iv.* These follower cells likely encountered distinct chemical gradients and ECM cues compared to the leader cells, resulting in different responses due to the heterogeneous tumor microenvironment (TME) within the tissue. In contrast, cluster *iv* cells displayed a flat and elongated morphology with prominent lamellipodia and filopodia, reminiscent of mesenchymal leader cells[45,46] at the invasion front, and were surrounded by areas with relatively low glia cell density (**Figure 5E, Supplementary Video 4**), These cells showed strong polarity, characterized by F-actin-rich lamellipodia that actively and persistently explored their surroundings and thereby had multiple contacts with surrounding cells, such as astrocytes (**Figure 5F**). Notably, migrating tumor cells with the highest motility appeared to actively avoid or reduce contact with mCherry-positive glial cells, exhibiting migration paths that circumvented the glial networks (**Extended Data 4B-C**).

B7-H3 localized to leading edge of explorative and invasive tumor cells

We next investigated whether PHIROS could be utilized to study the behavior of tumor-associated surface molecules within a tissue context. To this end, we engineered ONS-76 cells to express the transmembrane protein B7-H3/CD276, fused with mNeon-Green (ONS-76-B7-H3-mNG, **Figure 6A**). B7-H3 is highly expressed in malignant pediatric brain tumors, including MB, and is a validated target for CAR-T cell therapies[47,48]. In tissue-invading tumor cells, B7-H3-mNG was prominently localized at the leading edge and along the plasma membrane (**Figure 6A-B**). We observed both dynamic and static cell-cell contacts. Dynamic contacts were defined as cell-cell interactions that formed transiently during a randomly chosen observation period of 30 min, whereas static contacts are those that persisted throughout the same 30-min period. A rapid increase in B7-H3 intensity was detected at the contact sites of dynamic cell-cell interactions, whereas the B7-H3-mNG signal at static contacts remained relatively stable (**Figure 6C**). Quantification of relative mNG fluorescence across the lamellipodia of invading cells confirmed a pronounced enrichment of B7-H3 at the leading edge (**Figure 6D**). This polar distribution and accumulation of B7-H3 at the leading edge was maintained in individual cells for at least 24 hours (**Figure 6E**).

If B7-H3 were involved in lamellipodial guidance of the tumor cells, we would expect its persistent accumulation at the leading edge of tissue-exploring cells. Indeed, B7-H3-mNG fluorescence was persistently detected at the tip of a TME-exploring lamellipodium (**Figure 6F, Extended Data 6A**), and stable high mNG fluorescence, indicative of high levels of B7-H3 expression, was also maintained at the leading edge of invading cells (**Figure 6G, Extended Data 6B-C**).

Discussion

In this work, we introduced PHIROS, a dynamic platform for long-term, high-resolution imaging of organotypic slices. The platform enables two culturing methods of organotypic-slice-based models: (i) a static air-liquid interface (ALI) culturing phase for tissue recovery and reorganization, and (ii) perfusion culturing in a closed environment for multi-day confocal imaging under aseptic conditions. The platform was realized using inert and biocompatible plastic materials to avoid potential ad- and absorption issues related to the use of soft polymers, such as PDMS, typically employed in microfluidic prototyping[49].

Our results showed that the cerebellar slices reorganized and featured a continuous Purkinje cell layer, flanked by the molecular and granule cell layers, indicating good tissue health during ALI culturing. Furthermore, tissue functionality under pulsatile perfusion conditions were corroborated by the spontaneous and sustained astrocytic calcium dynamics over 48 hours in

the closed chamber. Importantly, maintaining the slices in a closed chamber and on the stage of a confocal microscope enabled monitoring the same cells over multiple days, which paves the way to single-cell investigation in a tissue context for extended periods of time.

We used the system to visualize the invasion of medulloblastoma cells into cerebellar slices, i.e., in a physiologically relevant tissue context. With our platform, we were able to visualize complex and heterogeneous F-actin polymerization dynamics of invading and non-invading tumor cells, and how the cells use this mechanism in sensing and navigating the TME. The combination of single-cell observations and cell velocity analysis suggested that distinct clusters of MB cells could adopt specific behavior in response to their surrounding cues. Thus, TME-dependent phenotypic plasticity of the tumor cells could contribute to driving MB cell migration and TME modification. In our live-cell data, we observed tumor cells that featured long, actin-rich protrusions, which were either single cells at the tumor spheroid edge or cells in less motile clusters in the spheroid center. Some of the protrusions resembled tumor-microtube-like structures, which have been previously described in other brain tumors[38], and recently also observed in patient-derived xenografts of Li-Fraumeni SHH human medulloblastoma[50]. Furthermore, the visualization of B7-H3 dynamics in tissue-invading cells uncovered the polar and persistent accumulation of this cancer-associated molecule in TME-exploring tumor cell lamellipodia. Live cell imaging results indicated that - besides its immune-modulatory functions[51] - B7-H3 may also be involved in TME interaction and cell migration. Interestingly, when cancer spheroids were embedded in a 3D hydrogel environment, cells infiltrated the hydrogel radially as single cells [52], unlike the collective migration behavior we observed in a tissue context, which further confirms the importance of faithfully recapitulating the TME in migration studies

Finally, given its ability to monitor large, complex network events and cell dynamics over several days under tightly controlled environmental conditions, we consider PHIROS also valuable for neuroscience research, markedly expanding the experimental options of working with organotypic slices.

Acknowledgement

This work was financially supported by Innosuisse – the Swiss Innovation Agency- under grant 120.665 IP-LS. The authors acknowledge the Single Cell Facility (SCF) at D-BSSE of ETH Zürich for help and support, as well as Dr. Shreedhar Kumar, also at D-BSSE, and Dr. Bernard Ciraulo, University Children's Hospital Zürich, for support with data visualization.

Author contribution

J.B.P. designed and fabricated the platform, designed and performed all experiments, analyzed and interpreted tissue reorganization, tissue viability, hypoxia and calcium imaging data, pre-processed the tumor invasion data, and wrote the manuscript. M.S.L designed and performed experiments, interpreted tissue reorganization, analyzed calcium-imaging and tumor invasion data, and edited the manuscript. D.H. generated and validated the fluorescent cell lines. M.B. conceived the project, acquired funding, provided experimental advice and supervision of the experiments, analyzed tumor invasion and B7H3 accumulation data, and edited the manuscript. A.H. supervised the project, provided experimental advice and edited the manuscript. M.M.M. conceptualized the project, acquired funding, supervised the project, designed the platform, supported with experimental design and experiments, analyzed tissue viability and tumor invasion data, and edited the manuscript. All authors read and approved the final version of the manuscript.

Main figures

Figure 1: Platform design for long-term high-resolution imaging of organotypic slices

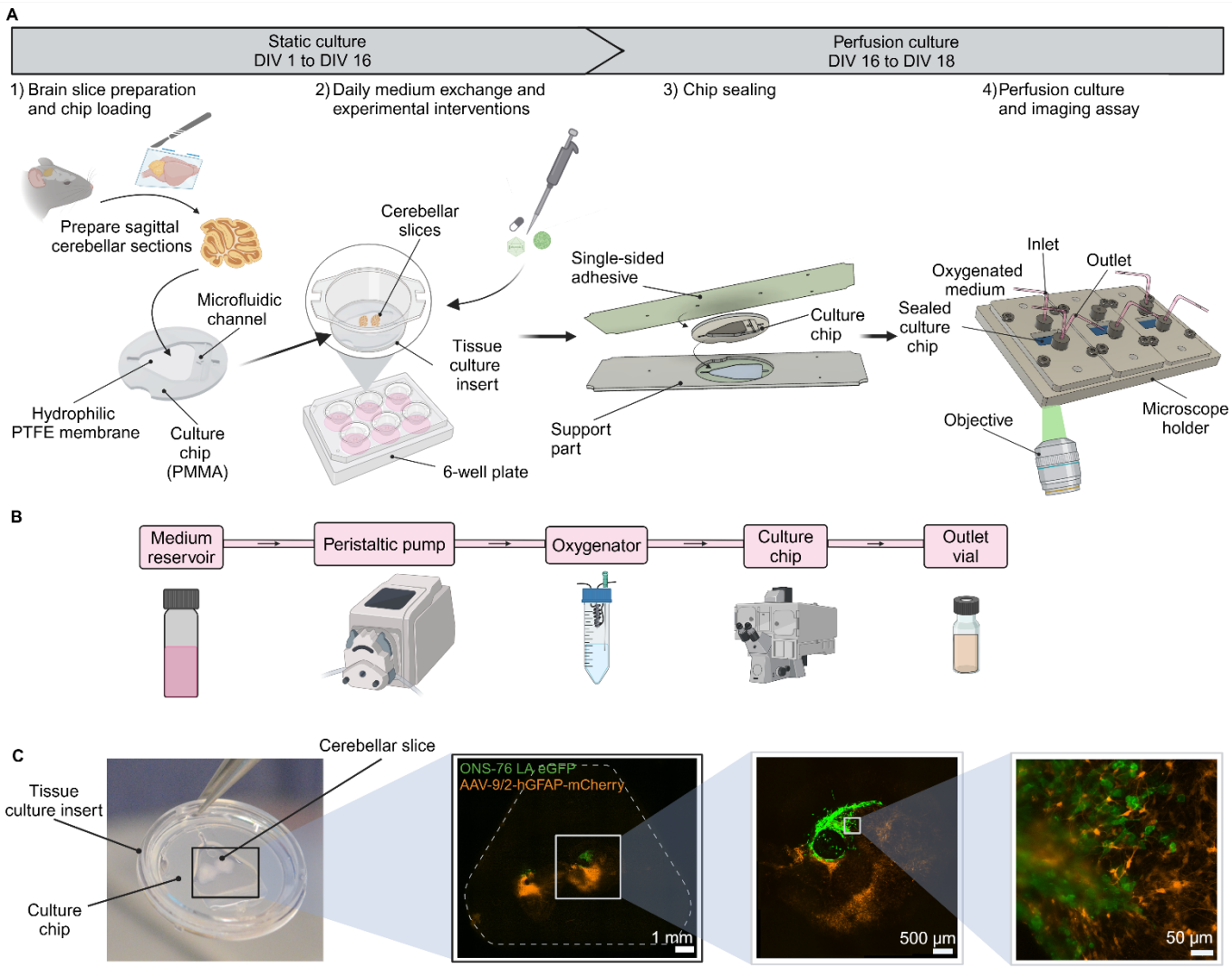

Figure 1: **(A)** Experimental set-up of the platform and workflow using mouse-derived cerebellar slices for a medulloblastoma co-culture model. An exploded view of the platform design in both static and perfused configuration can be seen in **Supplementary 1**. **(B)** Schematics of the used fluidic system to maintain healthy cerebellar slices on a spinning-disc confocal microscope. A peristaltic pump was used to drive the medium from the main reservoir to the oxygenator (gas-exchanger), buffering the medium to a pH of 7.4, and oxygenating the medium before it reaches the culture chip in the environmental box of the microscope**.** Close-up of the oxygenator and measured dissolved oxygen concentration can be seen in **Supplementary 2**. **(C)** A photo of the developed platform placed on top of a tissue culture insert with two cerebellar slices. The developed platform offers the possibility to investigate large scale events at 4X or 10X magnification as well as single-cell dynamics and interactions at 40X magnification. Images are showing maximum intensity projections at the respective magnification.

Figure 2 : Organotypic slices cultured on PHIROS represent complete cerebellar environment

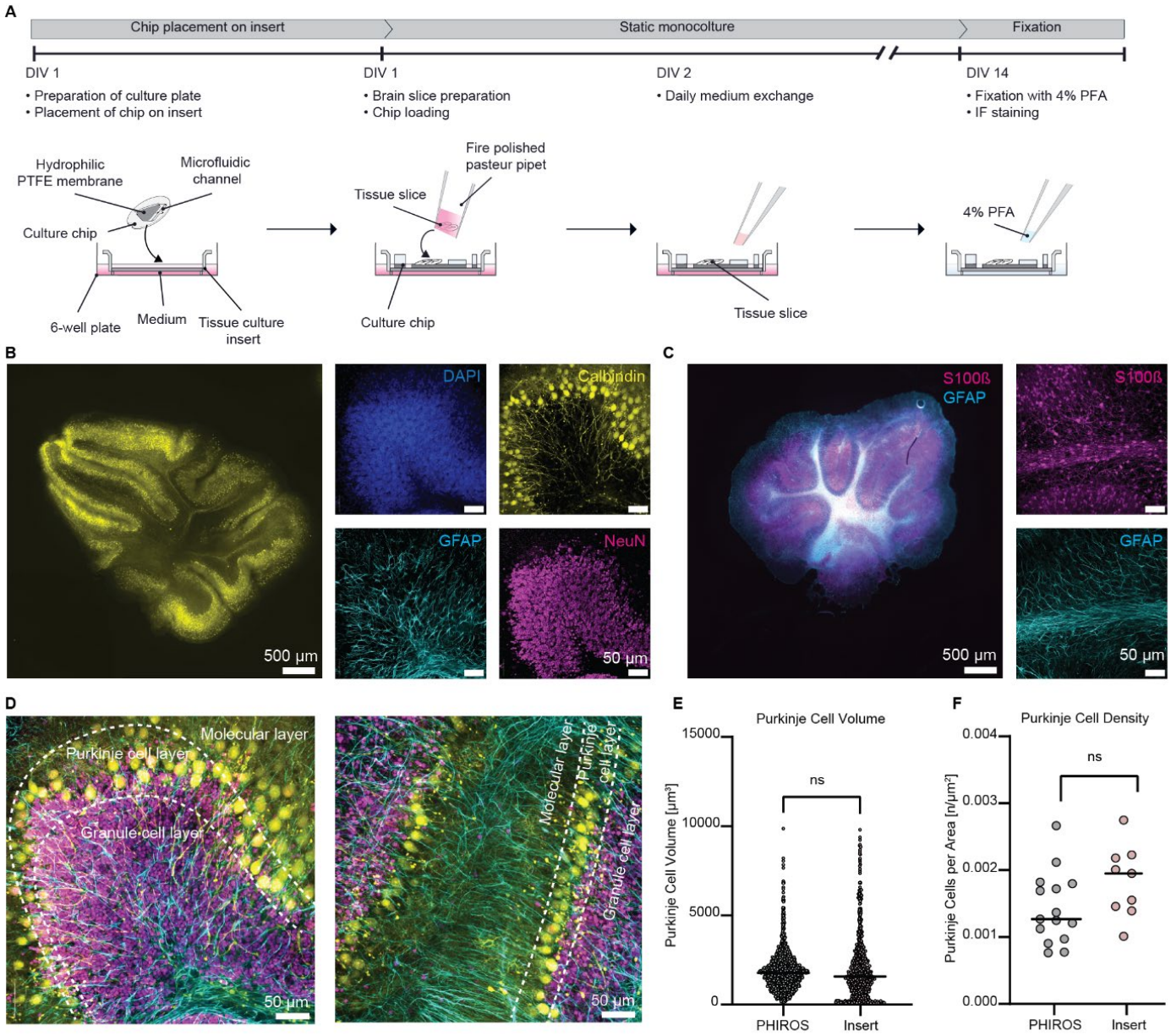

Figure 2: **(A**) Experimental design to assess tissue reorganization after slice preparation in the double-membrane culture as proposed for the platform. **(B)** Stitched image of a representative, whole cerebellar slice visualizing the integrity of the Purkinje cell layer marked in yellow using anti-Calbindin. The close-up shows immunostainings for anti-Calbindin (yellow), anti-GFAP (cyan) and anti-NeuN (magenta). **(C)** Stitched image of a representative cerebellar slice visualizing the distribution of astrocytes immunostained with anti-GFAP and S100β. **(D)** Composite image of the close-up in **B** and a second ROI between the lobules. **(E)** Quantitative comparison of Purkinje cell volumes between cerebellar slices cultured on chips (n= 6 chips, 1658 cells) and on inserts (n=3 inserts, 754 cells). **(F)** Quantitative comparison of Purkinje cell density per area between cerebellar slices cultured on chips (n= 6 chips) and on inserts (n= 3 inserts). Statistics for E and F were derived using an unpaired t-test with Welch's correction.

Figure 3: Perfusion culture with oxygenate medium supports tissue viability

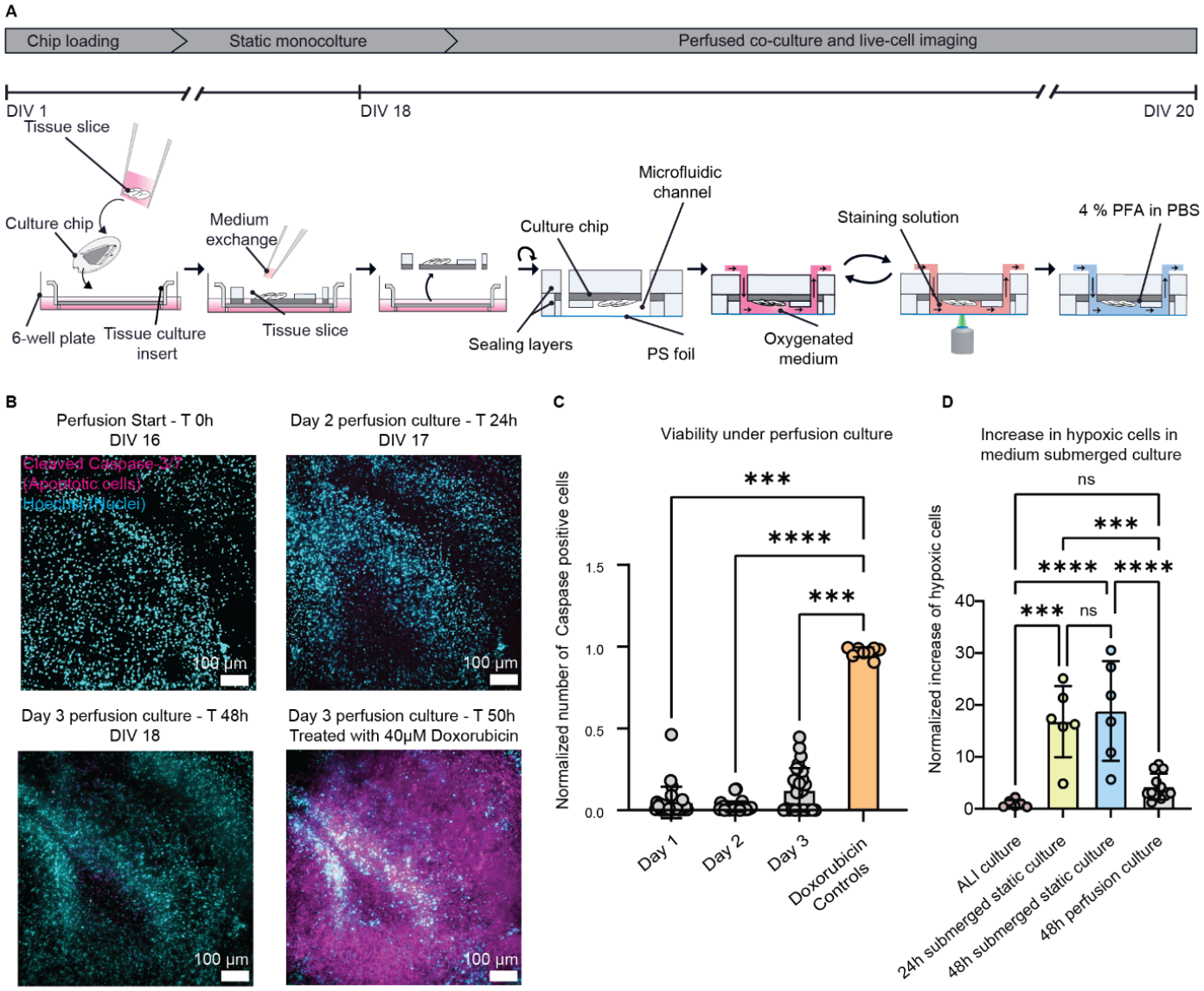

Figure 3: (A) Experimental layout used to determine tissue viability under perfusion. **(B)** Composite, maximum-projection images of the same slice stained for nuclei (cyan) and apoptotic cells (cleaved caspase 3-7, magenta) after perfusion start, 24h into the perfusion culture, 48h into the perfusion culture and 2h post exposure to 40 µM doxorubicin. **(C)** Quantitative assessment of caspase-positive cells (n = 6 chips/12 slices). **(D)** Quantification of hypoxic cells by using immunostaining for anti-HIF1-alpha and nuclear co-localization. We normalized with respect to hypoxic-cell counts found in normal ALI cultures. N = 4 slices per condition. Statistics for C and D were derived using 1-way ANOVA.

Figure 4: Spontaneous astrocytic calcium activity confirms tissue functionality

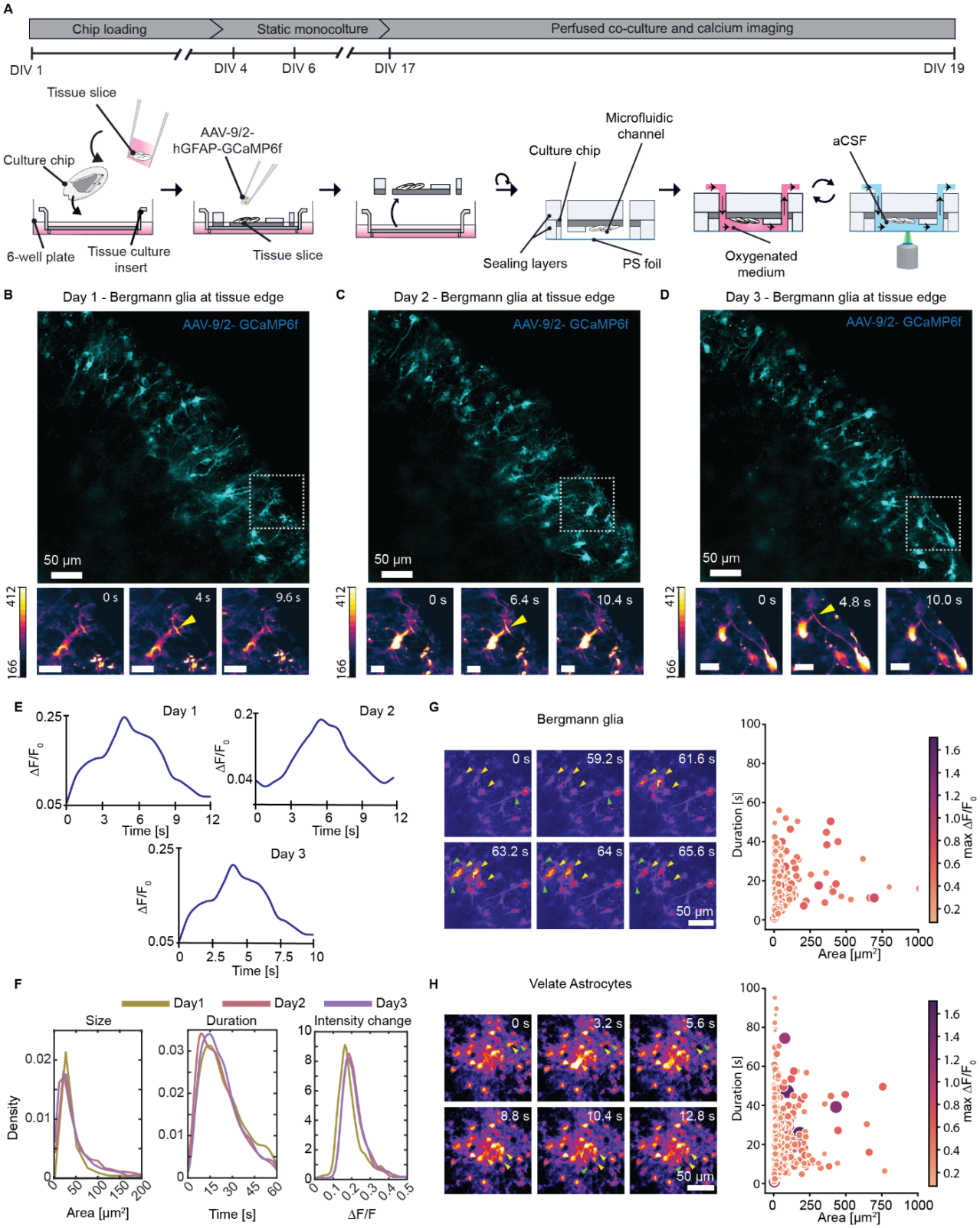

Figure 4: **(A)** Experimental layout to investigate intracellular calcium changes in cerebellar astrocytes; the static culturing period was used to label astrocytes through AAV transduction. Still frame of the same ROI during the calcium imaging assay from day 1 **(B)** to day 2 **(C)** to day 3 **(D)** of the perfusion culture. Close-ups show a calcium event indicated by the yellow arrow in the astrocytic process of likely the same cell. Scale bar of the close-ups is 20 µm. Graphs in **(E)** show the extracted fluorescence intensity changes of the depicted events in **B-D**. **(F)** Detected changes in calcium event area, duration, and changes in fluorescence intensity from day 1 to day 3 of the imaging assay (n = 4 slices, 3-4 ROIs per slice) visualized as probability density functions. Propagation of intracellular calcium changes in Bergmann glia (**G**) and velate astrocytes (**H**), in somas (yellow arrows) and processes (green arrows). The scatterplots show the relationship between intensity changes, duration and size of detected calcium activity spikes in Bergmann glia (n= 1334 events) and velate astrocytes (n= 2591 events) over the 48h recording period.

Figure 5: Dynamics of cell flow and single-cell trajectories in ONS76-LAeGFP spheroids influenced by astrocytes.

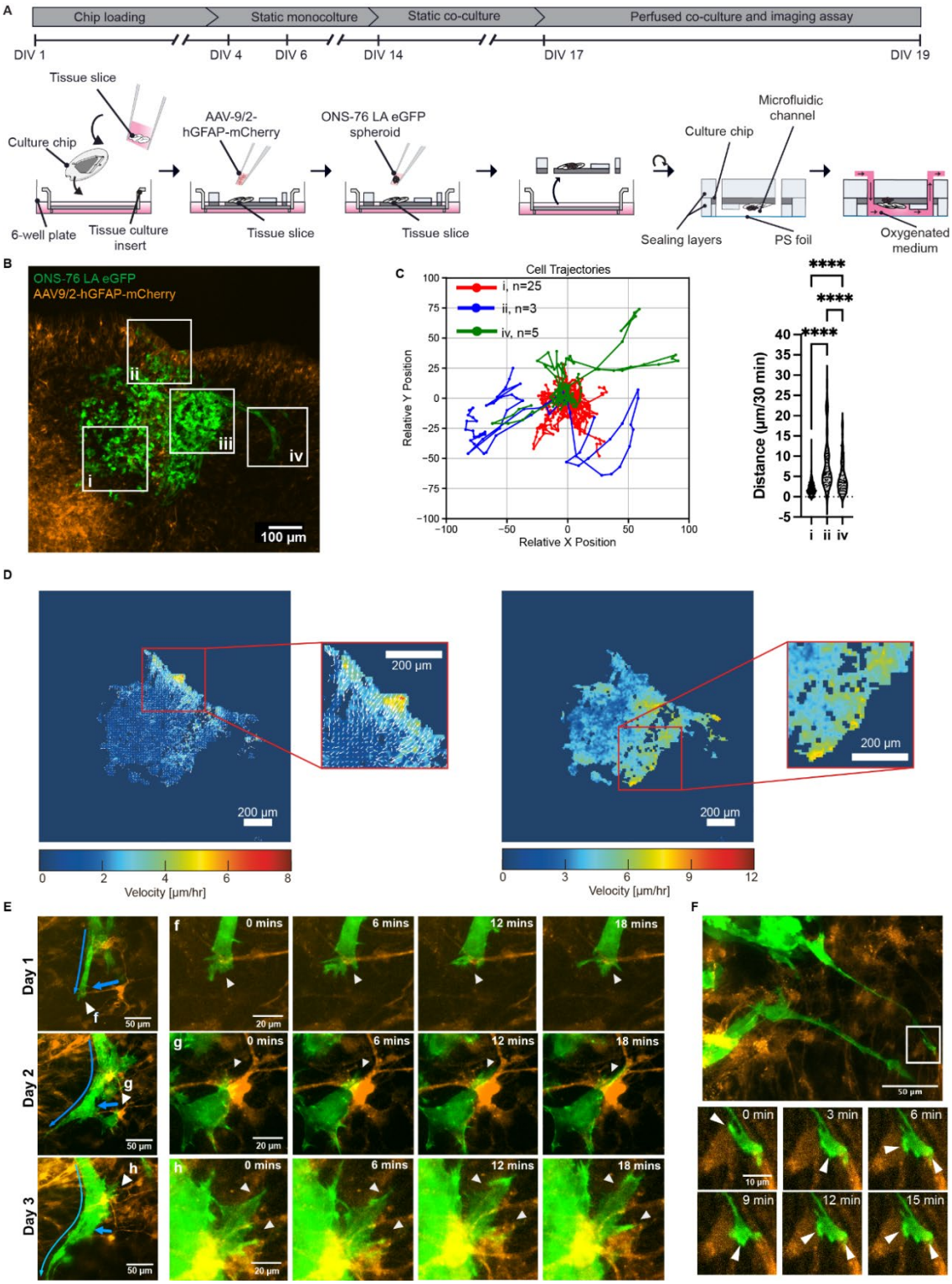

Figure 5: **(A)** Experimental workflow to establish the medulloblastoma co-culture model for high-resolution imaging assays. **(B)** Representative image showing the ONS-76-LA-eGFP spheroid (green) and astrocytes (orange) during 12-hour time-lapse imaging. Areas *i* and *iii* exhibit confined cell motility, while areas *ii* and *iv* show increased cellular movement. **(C)** Representative single-cell trajectories in areas *i* (25 cells), *ii* (3 cells), and *iv* (5 cells) and quantification of migration distances for clusters *i*, *ii,* and *iv*, plotted as displacement distance per interval. Each dot represents the migration distance (in µm) during a 34-min observation interval for a single migrating cell. **(D)** Heat maps display the mean velocity magnitude (left) and the standard deviation of the velocity magnitude across the spheroid over 12 hours, with yellow indicating higher and blue lower magnitudes. Arrows indicate the direction of motion, with arrow lengths indicating particle motion. Insets are 3x magnifications of areas highlighted with white squares. **(E)** Dynamics of astrocyte-tumor interactions at the invasion front (area *iv* in (B)) during a 30-minute short-term imaging over three consecutive days. Arrows indicate the movement direction relative to previous time points. Areas *f*, *g*, and *h* highlight tumor filopodia changes in contact with astrocyte processes or cell bodies during the 30-minute imaging. **(F)** Representative images of a tumor tightly interacting with an astrocyte over 12 minutes. Arrow heads indicate the progression of tumor-astrocyte contacts.

Figure 6: Persistent accumulation of B7-H3 at the leading edge of tissue-invading tumor cells.

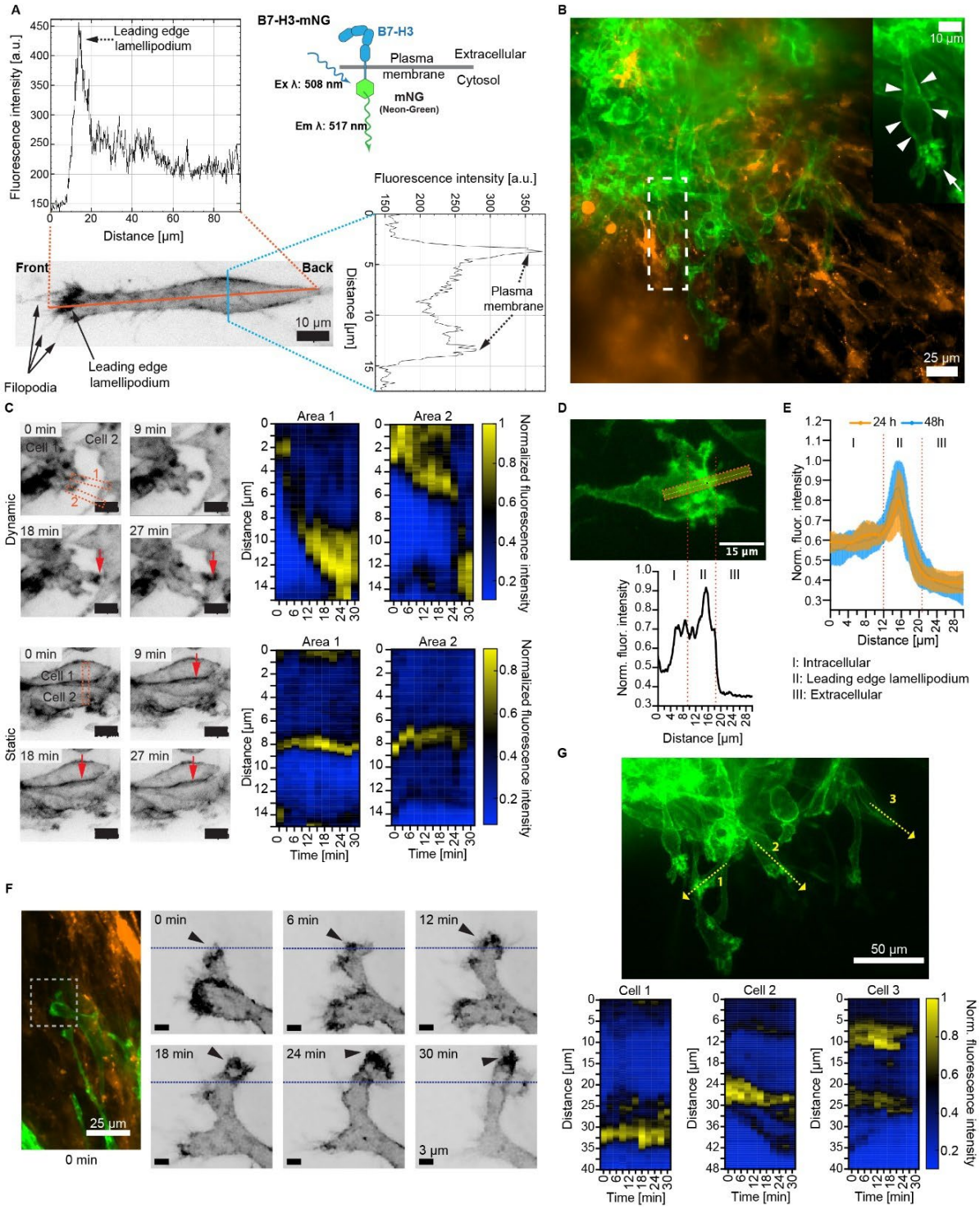

Figure 6: (A) Grayscale image of a polarized ONS-76-B7-H3-mNG cell on a tissue slice during perfusion culturing, two days after chip closure. The plot above the cell shows fluorescence values along the longitudinal profile (orange, horizontal line), while the plot on the right shows values of the cross-sectional profile (blue, vertical line). The schematic at the top right illustrates the B7-H3 fusion construct. **(B)** Maximum intensity projection of a confocal image stack after 48 hours of perfusion culture. Green: B7-H3-mNG; orange: GFAP-driven mCherry. The inset highlights the green channel, showing membrane-localized B7-H3 (arrowheads) and the leading-edge lamellipodium (arrow). **(C)** Dynamics of B7-H3-mNG at dynamic (top) versus static (bottom) cell-cell contacts. Heatmap kymographs show normalized fluorescence values along a 15-µm line (yellow dotted line) at cell-cell contacts, with arrows indicating B7-H3 accumulation. **(D)** Representative B7-H3-mNG fluorescence in tissue-invading tumor cells. Below: Normalized values of fluorescence intensity along a 30-µm line. **(E)** Normalized fluorescence values across leading-edge lamellipodia in cells invading during 24 hours (n=17) and 48 hours (n=21). **(F)** Left: Maximum intensity projection of confocal imaging after 48 hours of perfusion culture (green: B7-H3-mNG, orange: GFAP-driven mCherry). Right: Inverted grayscale of B7-H3-mNG fluorescence intensity shows lamellipodia dynamics over 30 minutes, with arrowheads indicating accumulation at the leading edge, whereas the initial position of the leading edge is visualized with a blue dotted line **(G)** Top: Green channel from image in B, with yellow-dotted arrows marking quantified areas of leading-edge lamellipodia. Bottom: Heat map kymographs show relative fluorescence values over 30 minutes along a 40–48 µm line across leading-edge lamellipodia in representative invading cells.

Extended Data

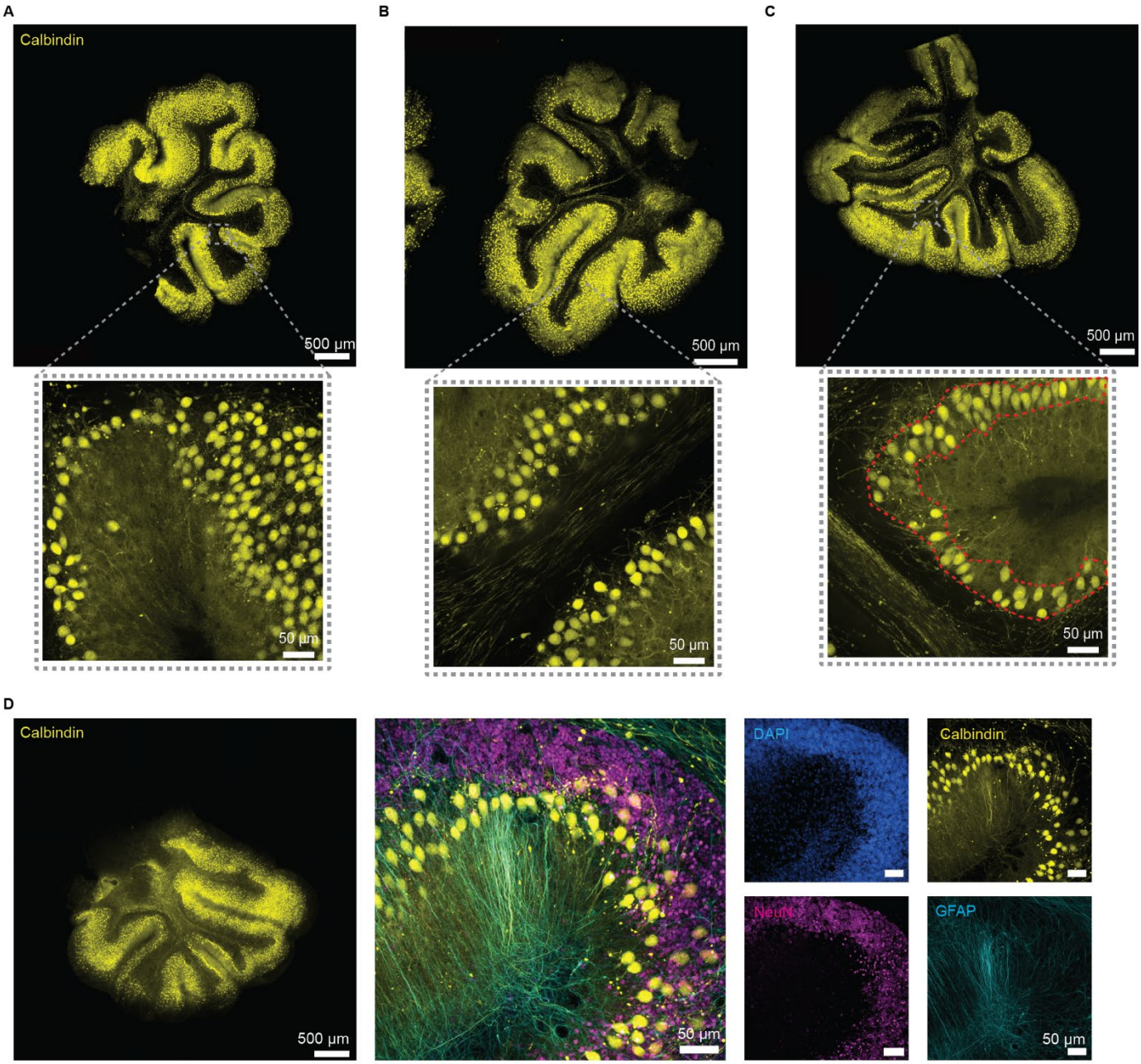

Extended Data 1: (**A-C**) 10X maximum intensity projections of the Purkinje cell layer of slices cultured on PHIROS stained with anti-Calbindin after fixation at DIV 14 of two additional experiments. Close-ups show 40X images of the Purkinje cell reorganization. The red line in close-up **C** indicates how the boundaries of the Purkinje cell layer were defined to assess and normalize the Purkinje cell density. (**D**) Purkinje cell reorganization after 14 days of culture where slices were cultured on the standard tissue culture inserts. The close-ups at 40X show that slices presented both neuronal cells, as indicated by the Calbindin and NeuN staining, as well as glial cells, as indicated by GFAP.

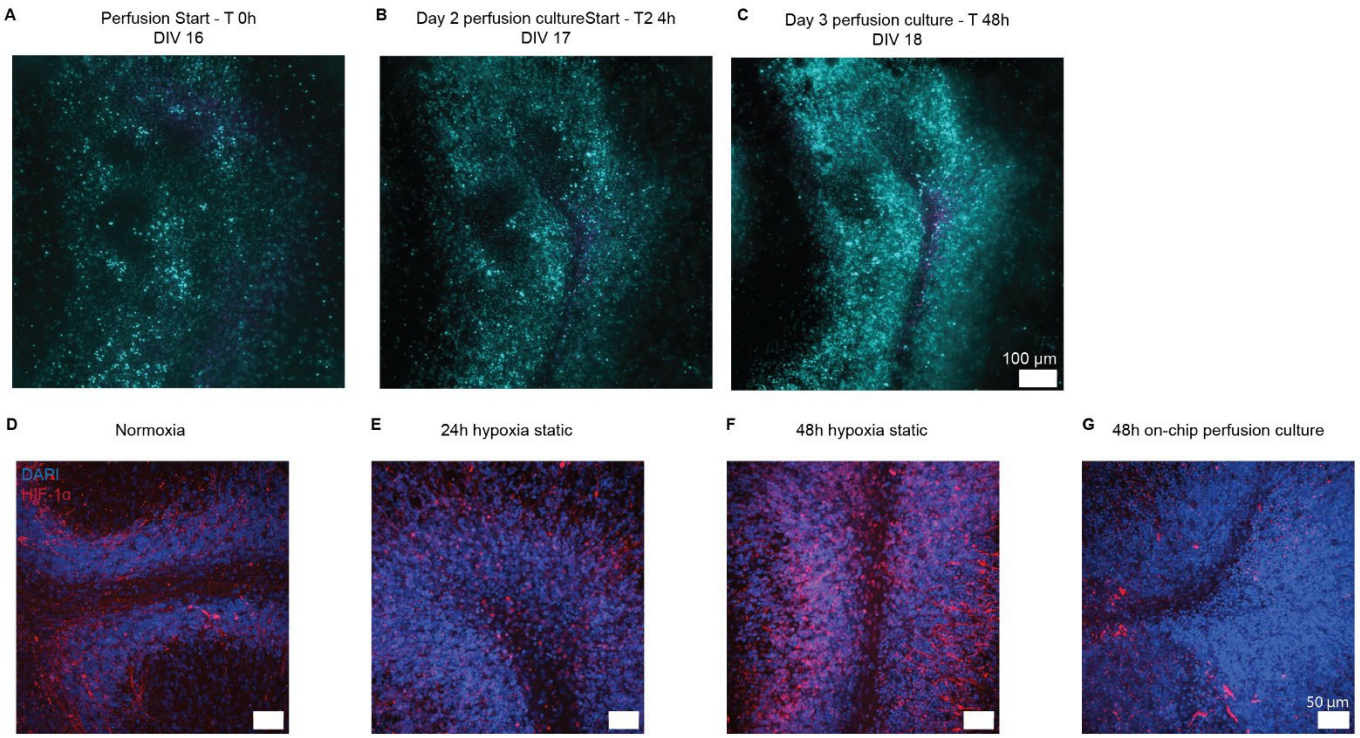

Extended Data 2: ROIs of different slices experiments from **Figure *3***. The images show a viability assessment using cleaved Caspase-3/7 stain labeling apoptotic nuclei co-stained with NucBlue. Images **A**-**C** show the same tissue slice after initiation of the perfusion culture (**A**), 24h into the perfusion culture (**B**) and at the end of the perfusion culture/imaging assay after 48h (**C**). Representative immunofluorescent staining for transcription factor HIF1-α and Nucleus of ALI cultured slices (**D**), slices cultured for 24h (**E**) or 48h (**F**) submerged under 2 ml of medium or for 48h under perfusion cultured on PHIROS (**G**).

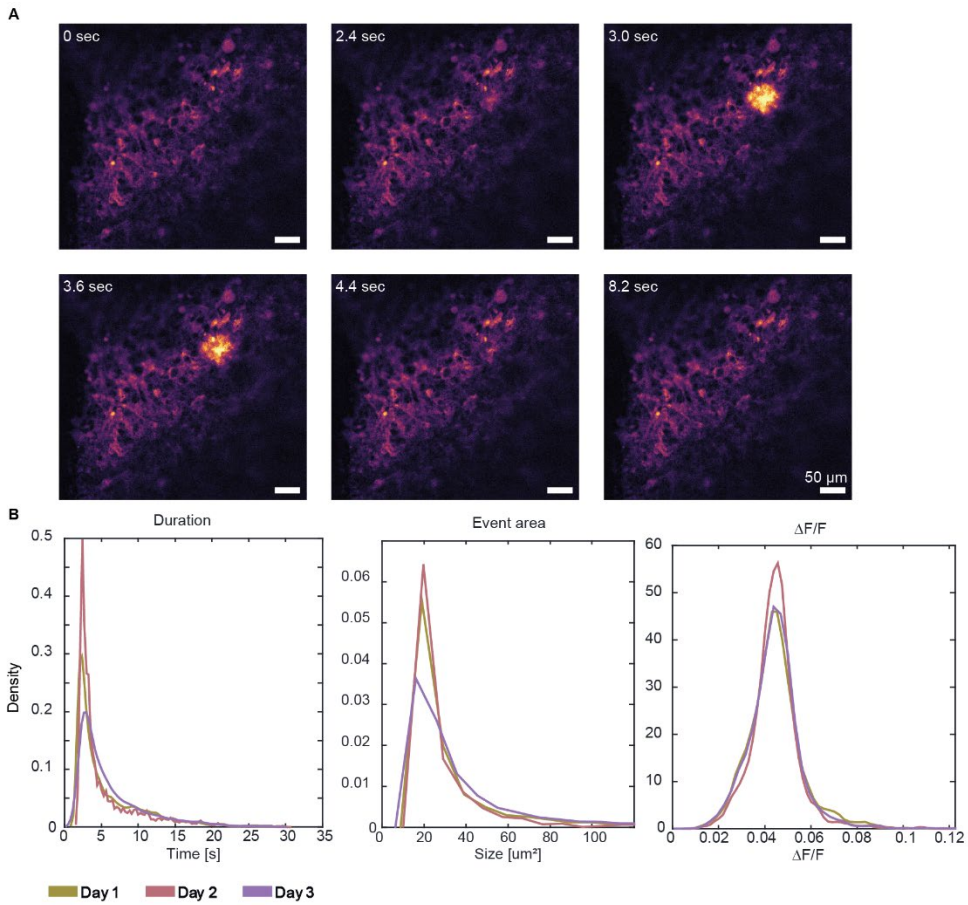

Extended Data 3: (A) Imaging quality and resolution achieved by using a 20X dry objective to record intracellular calcium changes in cerebellar astrocytes. **(B)** Changes in calcium event duration and area as well as differences in fluorescence intensity acquired with a 20X air objective during the three-day perfusion culture plotted as a probability density function. Due to the different optical setup, ΔF/F values were lower by a factor of ~10 when using the air objective owing to variations in the refractive index and an improved signal-to-noise ratio enabled by a refractive-index-matched objective.

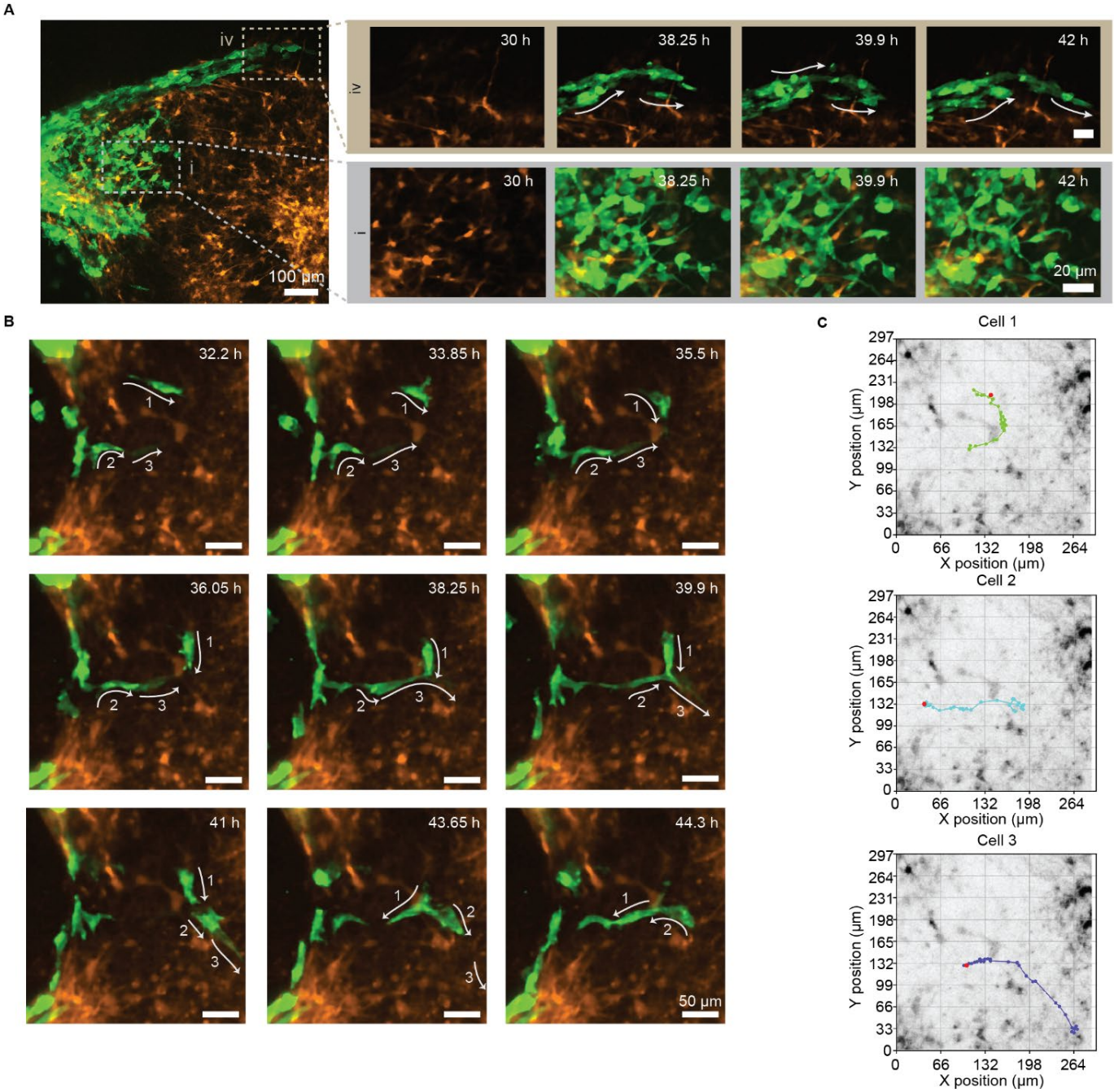

Extended Data 4: (A) Representative image showing tumor-astrocyte interactions during 12-hour time-lapse imaging. Area *iv* highlights a region with low astrocyte density (orange), where pronounced tumor cell movement (green) is observed (arrows indicate movement direction). Area *i* shows higher astrocyte density, where cell movement is minimal. Time refers to time after platform sealing; the scale bar of both sets of insets is 20 µm; **(B)** Example of repulsive and attractive interactions between tumor cells (green) and astrocytes (orange) over 14 hours. Movements of cells 1, 2, and 3 are shown with arrows representing their respective trajectories. **(C)** Individual cell trajectories on a background image show only astrocytes at the imaging starting point, illustrating movement patterns in relation to astrocyte density.

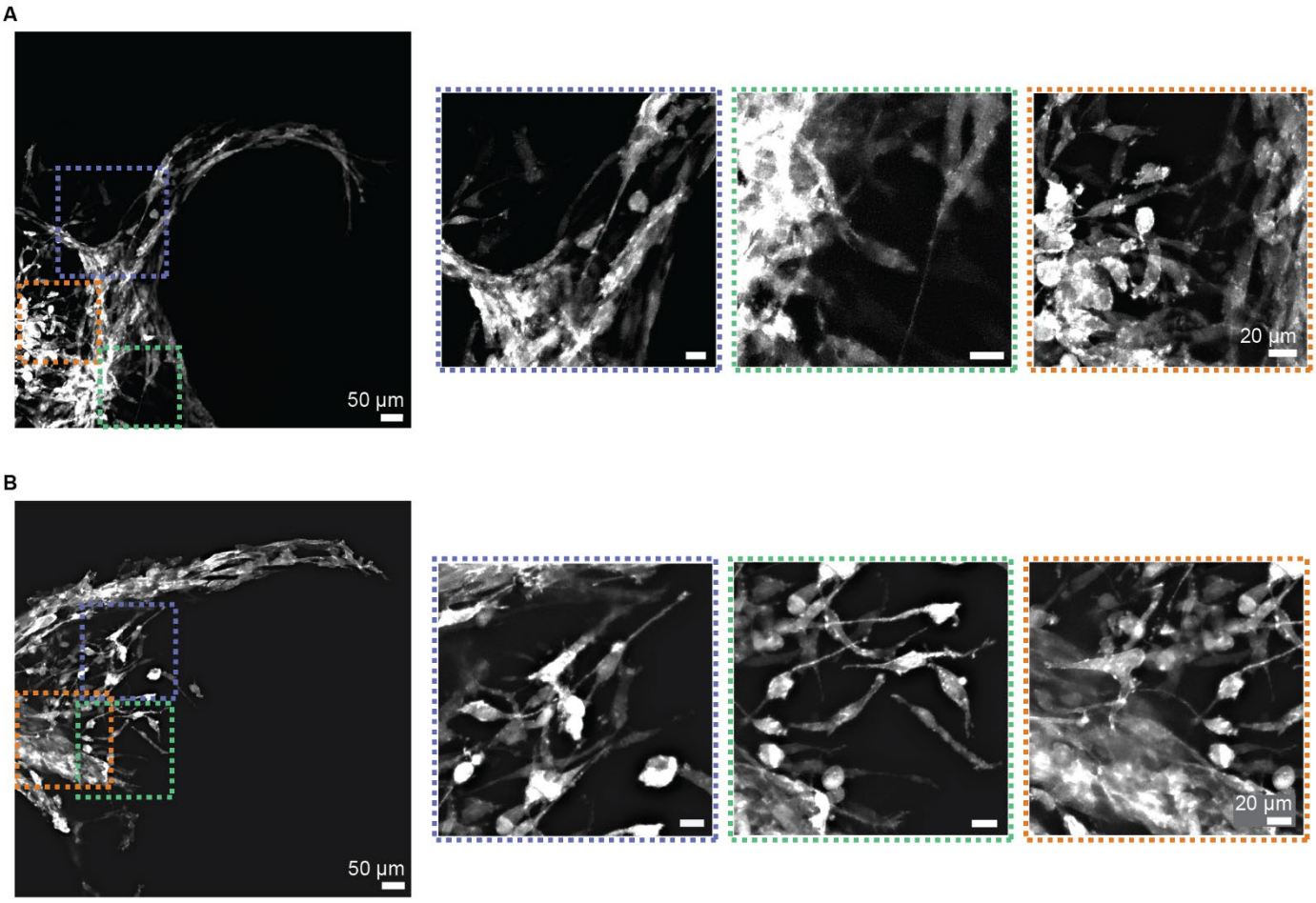

Extended Data 5: Representative images showing live observations of tumor cells interconnected through long, actin-rich protrusions in data from two independent experiments (**A-B**). Images show maximum intensity projections of still images. All scale bars in the close-ups are 20 µm.

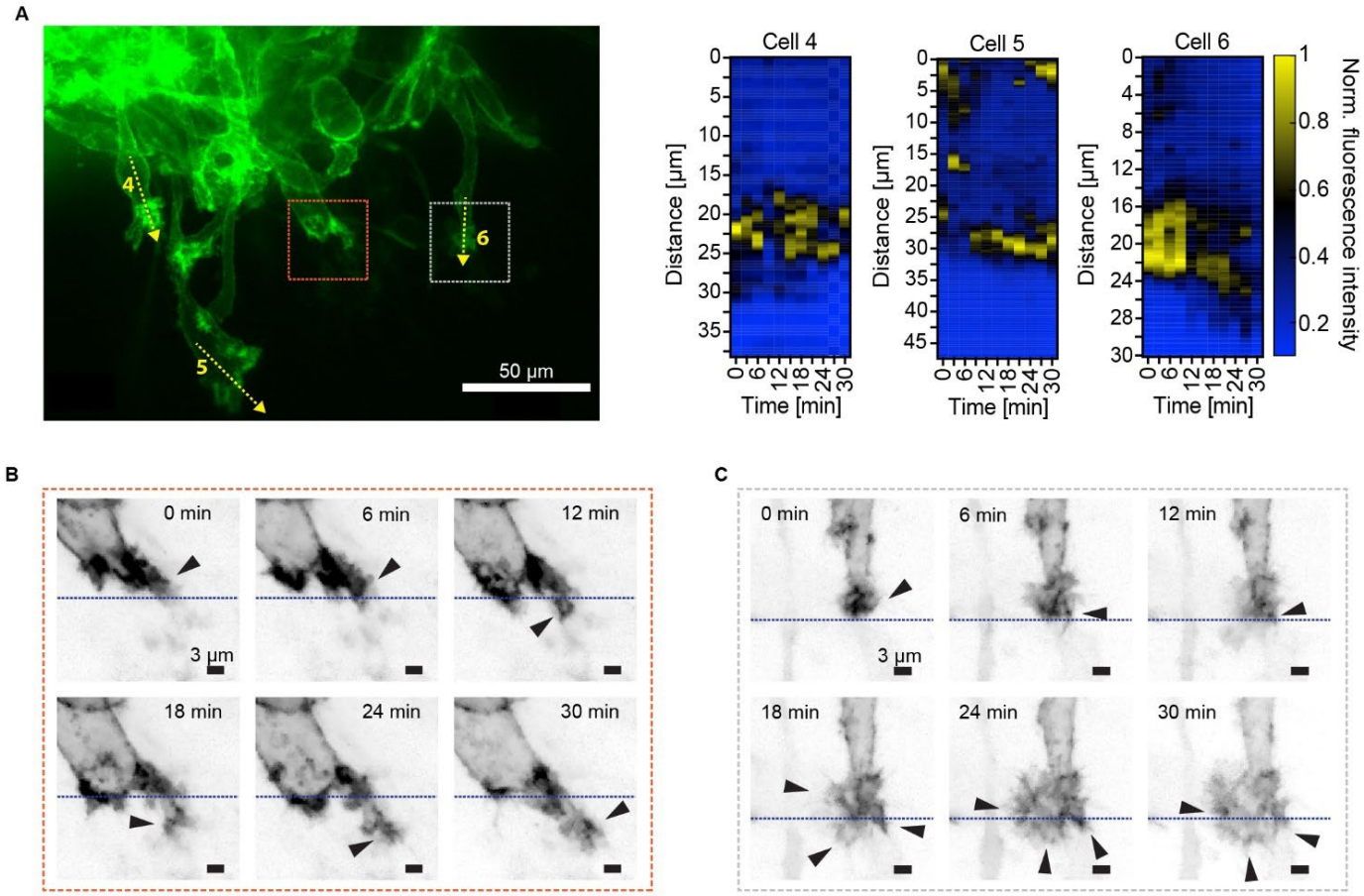

Extended Data 6: (A) Left: Green channel from the image in **Figure 6B**, with yellow-dotted arrows indicating additionally quantified areas of leading-edge lamellipodia. Right: Heat map kymographs show relative gray fluorescence values of the green fluorescent channel over 30 minutes along a 48µm line across leading-edge lamellipodia in representative invading cells, in addition to the cells shown in **Figure 6G.**: **(B-C) 6.**: **(B-C)** Inverted grayscale of B7-H3-mNG fluorescence intensity of two cells from **(A)**, indicated by the dotted bounding box. The images show lamellipodia dynamics over 30 minutes of acquisition, with arrowheads indicating accumulation at the leading edge. The initial position of the leading edge is visualized with the blue dotted line.

Supplementary Figures

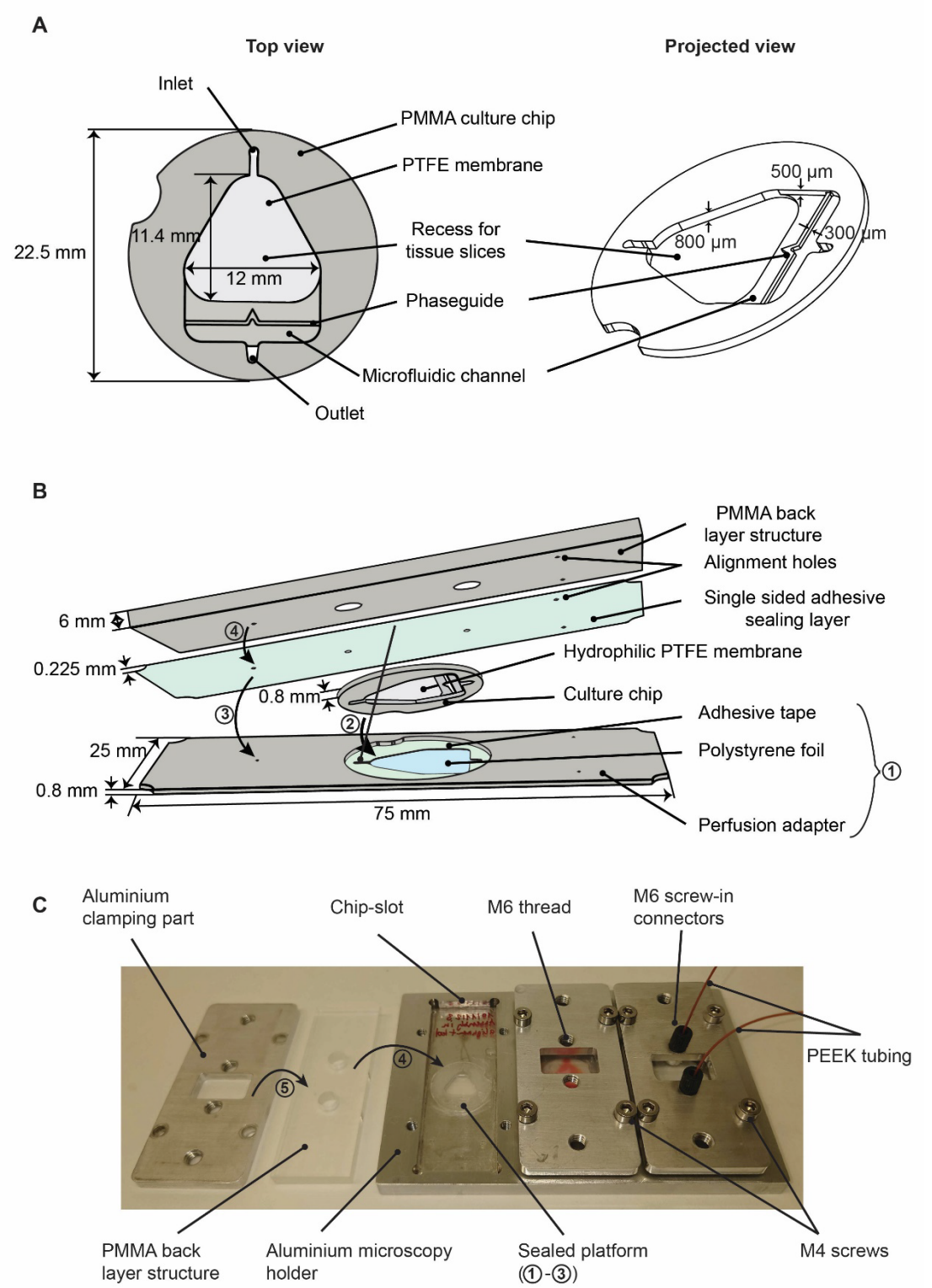

Supplementary 1: (A) Top view and projected view of the culture chip with channel dimensions. **(B)** Exploded view of the sealed platform. The perfusion adapter (1) is prepared beforehand, so that the culture chip can simply be snap-fitted into it (2) and sealed from the back. **(C)** Photograph of the pieces used to clamp the sealed platform in the microscopy holder and the fluidic connections.

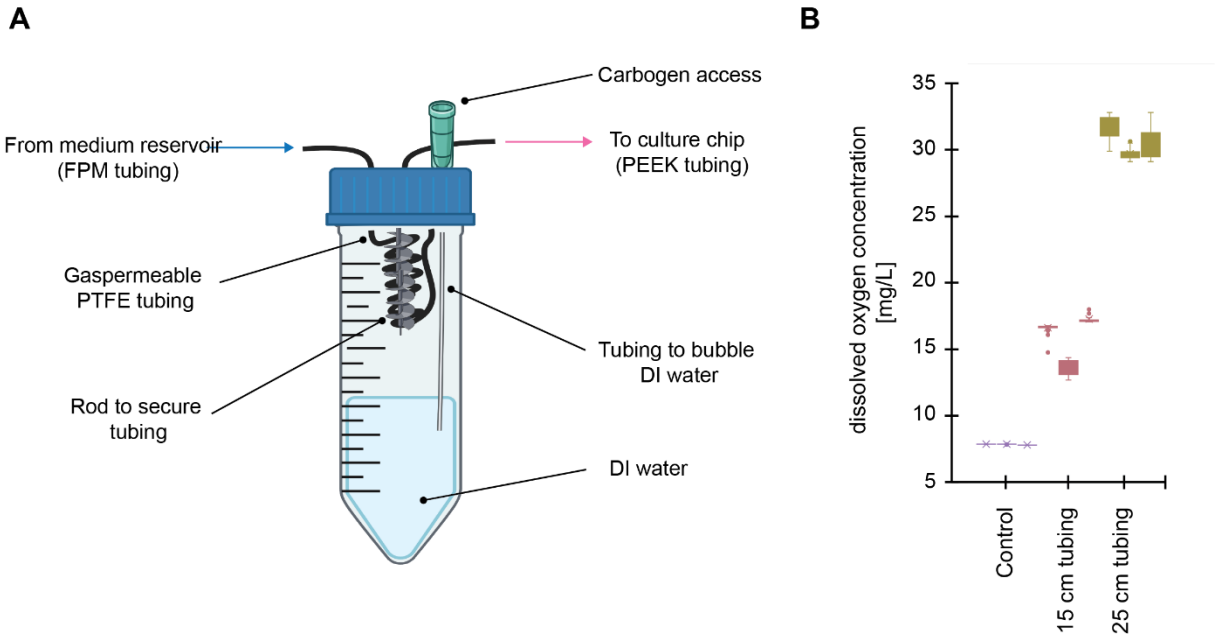

Supplementary 2: **(A)** Details of the oxygenator to buffer and oxygenate culture medium before the chip. Gas permeable tygon tubing was coiled in a 50-ml falcon tube, and the water in the falcon tube was bubbled with a 95% O_2, 5% CO_2 mixture. **(B)** Measured dissolved oxygen concentration in water at a flowrate of 10 µl/min with tubing lengths of 15 cm or 25 cm.

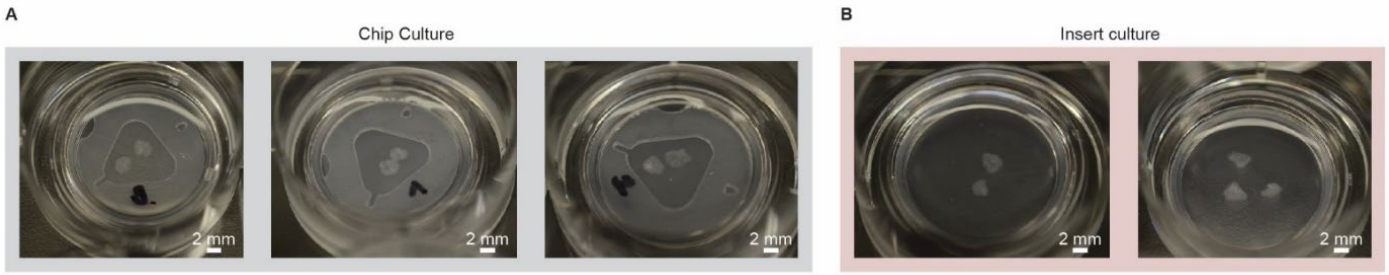

Supplementary 3: Transparency of cerebellar slices cultured in dual membrane cultures on chip (**A**) or on standard tissue culture inserts (**B**), where we observed similar translucency values.

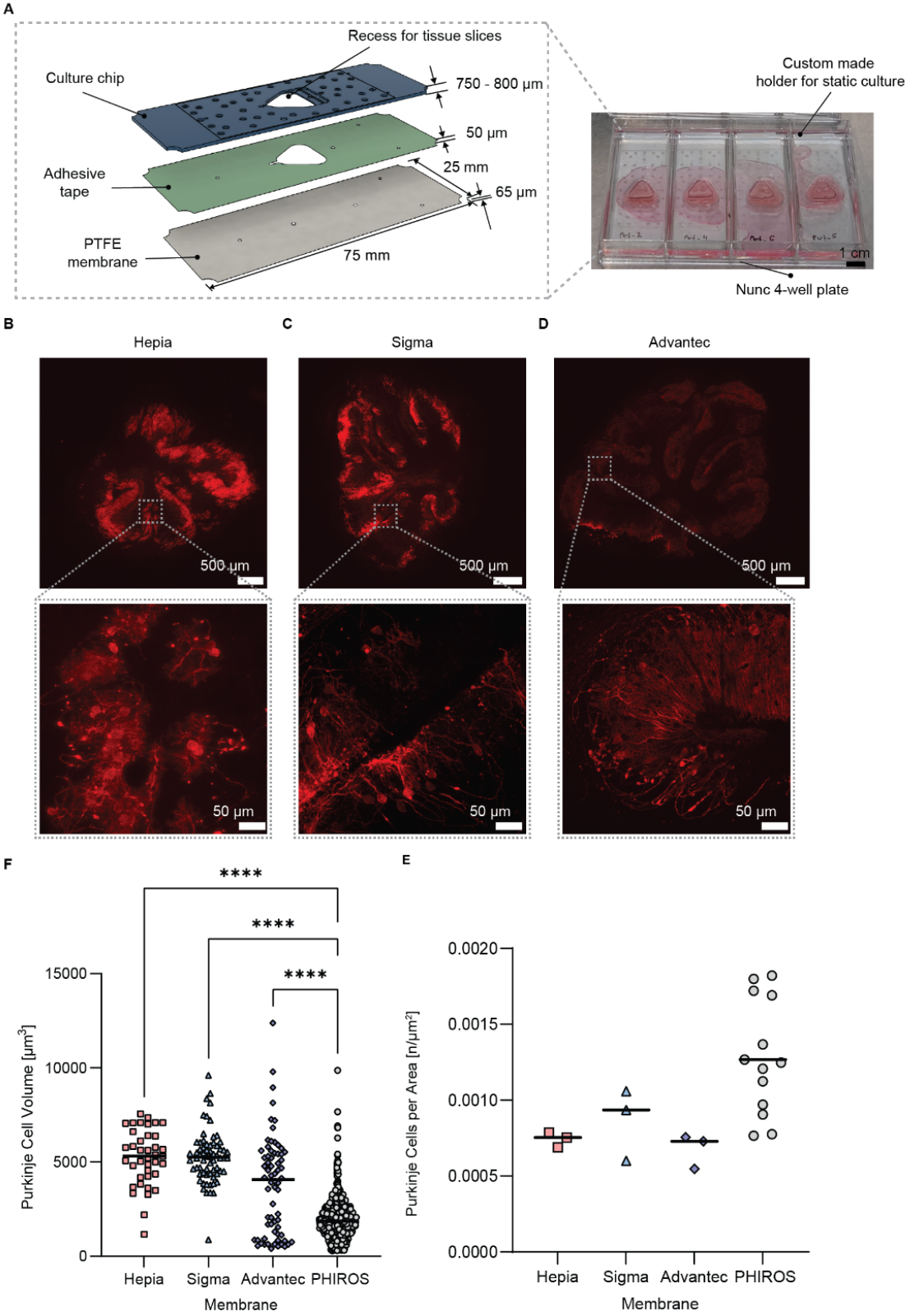

Supplementary 4: **(A)**: Schematic of a previous version of the culture chip design with glass slide dimensions (25 mm x 75 mm) using the same adhesive tape and hydrophilic PTFE membranes from various manufatureers. This previous prototype was placed on a custom-made holder in a 4-well plate during static culturing (photo on the right). **(B-D)** 10X large Image and 40X zoomed-in image of Purkinje cell layer reorganization on previous platform prototypes fabricated with different hydrophilic PTFE membranes The Purkinje cell layer was disrupted and showed larger Purkinje cell somas **(E)** and decreased Purkinje cell density **(F)**

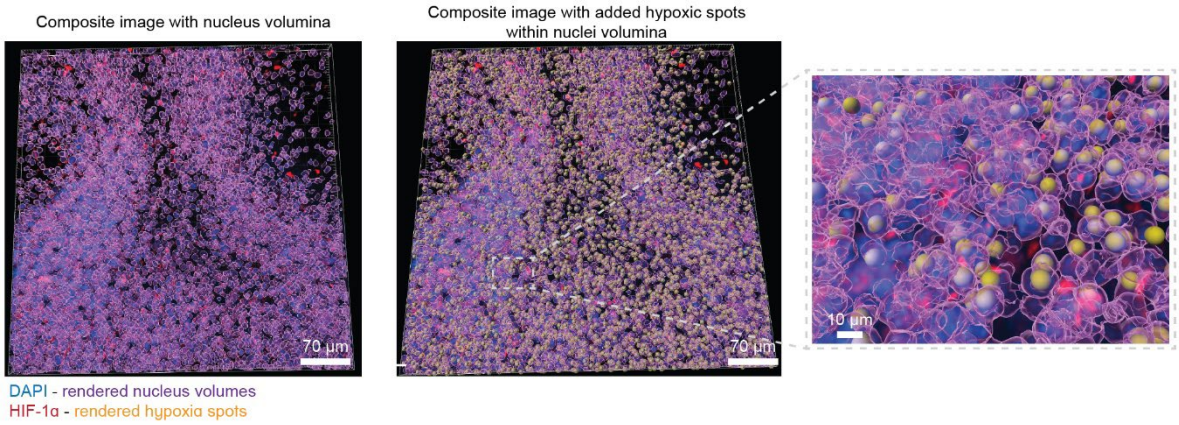

Supplementary 5: Used masks in Imaris to determine the number of hypoxic cells, here illustrated using a positive control, where brain slices were cultured fully submerged under 2ml of medium for 48 h.

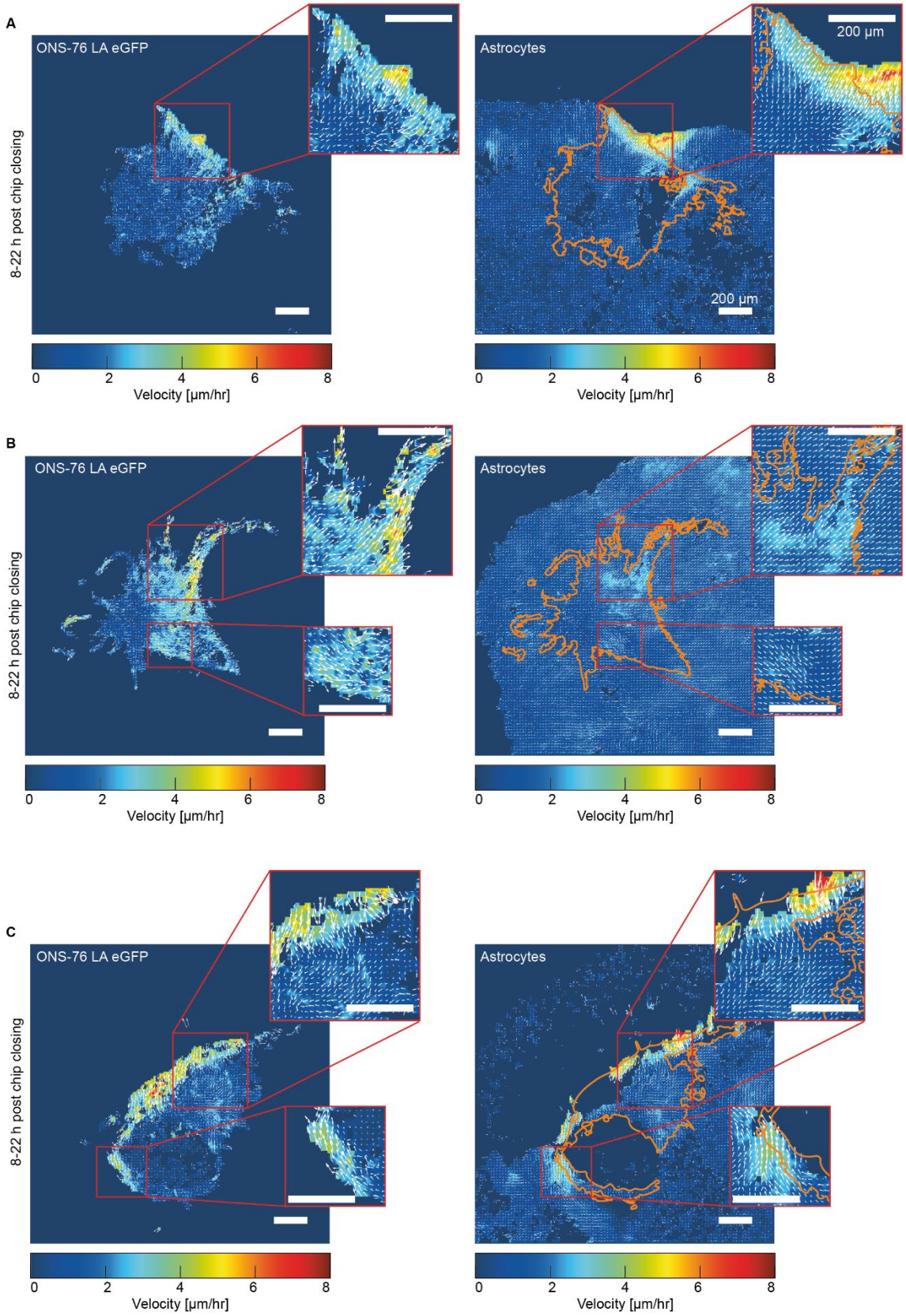

Supplementary 6: Average velocities calculated using PIVLab for both LA-eGFP ONS-76 medulloblastoma cells (left side) and mCherry-expressing astrocytes (right side). (**A-C**) show three different, independent experiments. Time refers to hours after platform sealing. Scale bar= 200 µm.

Methods

Platform fabrication

All parts of the platform were fabricated using standard rapid-prototyping techniques. Designs were created in Fusion 360 (Autodesk Inc., San Francisco, CA, United States). An exploded view of the chip and details of the assembly are shown in **Supplementary 1A**.

The culturing part of the platform, further referred to as "culture chip" featured an outer diameter of 22.5 mm and was fabricated through micro-CNC milling (Roland SRM-20) of 800 µm polymethylmethacrylate (PMMA) sheets as described elsewhere[53]. The channel width was 700 µm at both the inlet and outlet. To ensure a complete filling of the triangular shaped, 12-mm-wide and 800-µm-deep culture chamber, we incorporated a phase guide of 300 µm height at the outlet channel. The microfluidic channel had a depth of 500 µm. Inlet and outlet diameter were 800 µm. The double-sided adhesive tape (467-7952 MPL, 3M, Rüschlikon, Switzerland) was laser-cut using a CO_2 laser (Universal Laser System, Vienna, Austria). After bonding the adhesive tape to the PMMA part, chips were cleaned using a 40% ethanol solution, rinsed with deionized water, and then blow-dried using an air gun. We treated the phase guide with trichloro(1H,1H,2H,2H-perfluorooctyl)silane (448931-10G, Sigma-Aldrich, Buchs, Switzerland), diluted 1:100 in HFE (Novec 7000™, 3M, Rüschlikon, Switzerland), to increase its hydrophobicity. Subsequently, we covered the phase guides with 20 µl of PDMS prepared in a 1:10 ratio (Sylgard 184, Dow Chemical Company) to protect the phase guide during static culturing in the incubator. Next, the 0.4-µm-pore-size, hydrophilic PTFE biopore membrane (BGCM00010, Sigma-Aldrich, Buchs, Switzerland) was attached to the culture chip via the prepatterned double-sided adhesive. Before tissue culturing, chips were UV-sterilized in a cell culture hood for 20 min each side.

The PMMA and polystyrene parts (125 µm thickness, ST31-FM-000191, Goodfellow Cambridge Ltd., Huntingdon, England) used for connecting and sealing the culture chip were laser-cut using a CO_2 laser. The PMMA parts were then annealed for 1h at 80°C and subsequently cleaned by sonication in soap water for 3 min, followed by rinsing with 40% EtOH and DI water. All parts were finally sterilized with UV light for 20 min.

Perfusion setup

To perfuse the system, the culture chip was sealed on both sides to create a closed microfluidic network. First, a support component for the culture chip was assembled. The support part was formed by laser-cutting a PMMA sheet of the same thickness as the culture chip and sealed by a 125-µm-thick polystyrene foil. The PMMA and the polystyrene foil were bonded using double-sided tape, which had been previously patterned using a laser cutter (**Supplementary 1B**, step 1). The PDMS of the phase guide in the culture chip was then removed, and the culture chip was inserted into the support part, which yielded an assembly with standard microscopy-slide dimensions and facilitated fluidic connections and handling (**Supplementary 1B**, step 2). Finally, the back part of the culturing chip was sealed with a single-sided adhesive layer consisting of the same double-sided tape and the polystyrene foil, in which openings for fluidic inlet and outlet had been laser-cut (**Supplementary 1B**, step 3). The sealed and assembled chip was then inserted into a custom-made aluminum holder, and a support PMMA structure was used to connect and hold the tubing (**Supplementary 1C**, step 4-6). The sealing procedure was carried out in a sterile cell-culture hood.

Experimental setup

Three chips were connected and imaged simultaneously; each chip was connected to its own medium reservoir, which enabled to use each chip with specific experimental conditions during one imaging assay. The sealed chips were connected to the fluidic system at the Nikon Eclipse

Ti2-E microscope (Nikon Europe B.V., Amsterdam, Netherlands) equipped with an X-Light V3 Spinning Disk (CrestOptics S.p.A) module. An environmental stage-top incubator (Life Imaging services, Basel, Switzerland) ensured that the system was kept at 37°C during imaging. A peristaltic pump (ISM931C, Ismatec) was used to drive the fluids. A pulsated flow (7-minute flow intervals at 10 µl/min, 61 minutes pause) was applied.

To avoid uncontrolled gas exchange in the tubings, gas impermeable tubings were used to connect the medium reservoirs to the oxygenator and the oxygenator to the chip. A combination of different tubings was used to connect the different components: Fluorine kautschuk material (FPM) tubing (0.5mm ID, 302631, Reichelt Chemietechnik, Heidelberg, Germany), and polyvinyl chloride (PVC) peristaltic pump tubing (0.25 mm ID, N0773117, PerkinElmer, USA) from the medium reservoir to the oxygenator, polyether ether ketone (PEEK) tubing (0.5 mm ID, CIL-1569, IDEX, Northbrook, Illinois) from the oxygenator to the chip. We glued FPM o-rings (1 mm ID, 860404.0003, Brütsch & Rüegger, Urdorf, Switzerland), to the ferrule (P-248X, IDEX) to provide stable and leak-free connections to the chip. For the outlet tubing, we used poly(tetrafluoroethene) or PTFE tubing (0.4 mm ID, S1810-06, Bola, Grünsfeld, Germany). All tubes were flushed with DI water, followed by 70% ethanol and DI water rinse before use.

The oxygenator consisted of a 50 ml Falcon tube (227261, Greiner Bio-One, St. Gallen, Switzerland) with gas-permeable, 0.4-mm-ID PTFE tubing (S1810-06, Bola, Grünsfeld, Germany) coiled within the Falcon tube. The Falcon tube was partly filled with DI water, which was constantly bubbled with Carbogen to saturate the Falcon environment with humidified Carbogen gas and provide effective gas exchange through the gas-permeable tube. The tube volume within the Falcon tube was 31 µl.

A custom-made Matlab script was used to control the peristaltic pump and automate the stop-flow perfusion scheme.

Oxygen Measurements

The dissolved oxygen concentration in the medium was measured with a fiber-based oxygen sensor (OXR50-OI, Pyroscience, Aachen, Germany). All oxygen characterization measurements were conducted at a flow rate of 10 µl/min and after an equilibration period of 5min. Oxygen concentrations were measured at the end of the poly(etheretherketone) or PEEK tubing. Measurements were taken for 1min at a sampling frequency of 1Hz and repeated thrice per tubing length.

Cerebellar slice culture

Animal experimentation for mouse brain tissue harvesting was approved by the veterinary offices of the cantons of Basel and Zurich according to Swiss federal laws on animal welfare and carried out in accordance with the approved guidelines.

Sagittal cerebellar brain slices were prepared as described previously[54]. Briefly, wild-type C57BL/6JRj mice pups were sacrificed at P8–P12 by decapitation following isoflurane anesthesia. Cerebella were harvested and placed in cold Gey's balanced salt solution (G9779, Sigma-Aldrich) containing kynurenic acid (K3375, Sigma-Aldrich), here referred to as GBSSK. Cerebella were then embedded in sagittal orientation in 2% low melting point agarose (A9414, Sigma-Aldrich) prepared in GBSSK. The solidified agarose block was glued onto the vibratome disc (VT 1200 S, Leica) using super-glue. Next, the disc was mounted in the vibratome chamber, filled with cold GBSSK, and 350-µm-thick slices were cut at a speed of 0.2 mm/s and an amplitude of 1.1mm. After removal of excess agarose around the slices, the slices were transferred to petri dishes filled with fresh, cold GBSSK on ice.

424 The cerebellar slices were then transferred to either standard cell-culture inserts (PICM0RG50,
425 Sigma-Aldrich), or the culture chips which were placed on cell-culture inserts in 6-well plates
426 with 1 ml of brain slice medium (BSM, described as slice culture medium in [54]). We used fire-
427 polished glass Pasteur pipets to place a maximum of three slices per culture chip or insert.
428 Medium was exchanged daily, except for the day following AAV transduction, when medium
429 exchange was not performed. Slices were cultured in a humidified incubator with 5% CO_2 at
430 37°C.

431 **AAV transduction**

432 Adeno-associated viruses (AAVs) were obtained from the viral vector facility of the University
433 of Zurich. We used i) ssAAV-9/2-hGFAP-hHBbI/E-GCaMP6f-bGHp(A) at 2 x 10^9 vg and ii)
434 ssAAV-9/2-hGFAP-mCherry-WPRE-hGHp(A) at 2 x 10^9 vg to specifically label astrocytes in
435 the cerebellar slices. Viruses were diluted in PBS to achieve the indicated final viral titer
436 concentration in a volume of 5 µl PBS. On DIV4 and DIV6, 5 µl of the prepared virus solution
437 were carefully pipetted on top of each slice during the daily medium exchange. Slices were
438 kept in the cell-culture hood for an additional 10 min following the transduction before bringing
439 them back in the incubator.

440 **Cell Culture**

441 ONS-76 LA-eGFP and ONS-76 B7-H3 B7-H3-mNG cells were cultured in RMPI-1640
442 medium (R0883, Sigma), supplemented with GlutaMax (#35050-038, Gibco), 10% FBS
443 (S0615, Sigma) and 1% penicillin/streptomycin (#15140-122, Gibco). Cells were passaged at
444 80% confluency and regularly tested for mycoplasma.
445 Spheroids were formed 48 h before the initiation of the co-culture by seeding 2'500 cells per
446 well in 96 U-bottom well plates (NuclonTM SpheraTM 96-Well, Thermo Fisher Scientific). The
447 spheroids were formed in neurosphere medium, adapted from[55] by using 100 µl medium per
448 well and containing 2% B27 (17504044, Gibco), 1% N2 (17502-048, Thermo Fisher Scientific),
449 2 µg/ml Heparin (07980, Stemcell Technologies, Basel, Switzerland), 20 ng/ml EGF
450 (PHG0315, Gibco), 10 ng/ml bFGF (PHG0360, Gibco), 1 % penicillin-streptomycin (15140148,
451 Thermo Fisher Scientific) in DMEM-F12 (11330032, Gibco). Cells and spheroids were cultured
452 in a humidified 5% CO_2 incubator at 37 °C.

453 **Generation of fluorescent protein expressing cell lines**

454 Origin, maintenance and use of ONS-76 cells in cerebellar slice culture were described in[31].
455 Stable ONS-76 cells expressing lifeact-enhanced green fluorescent protein (LA-eGFP) or
456 human B7-H3/CD276 fused to mNeon-Green (B7-H3-mNG) were generated by lentiviral
457 transduction. The lentivirus was generated using HEK293 T cells transfected with the lentiviral
458 packaging vectors pPax2 (4.5 µg), the coat protein vector pVSVG (3 µg), and either a lentiviral
459 vector encoding lifeact[56] fused to EGFP or B7-H3-mNG
460 (https://en.vectorbuilder.com/vector/VB220316-1594xpv.html) (7.5 µg). Virus supernatant was
461 harvested 30 h after the transfection and filtered through a 45-µm filter. ONS-76 were
462 transduced in standard 6-well plates with 1 ml of the supernatant supplemented with Polybrene
463 (ThermoFisher Sientific, 1:1000). The transduced cells were cultured in complete growth
464 medium and expanded. Two days after transduction, puromycin selection was started.
465 Selected cells were FACS-sorted to generate a pure population of LA-EGFP or B7-H3-mNG
466 expressing cells.

467 **Validation of B7-H3-mNG surface expression by flow cytometry**

468 6 x 10^5 ONS-76 MB cells were seeded in standard 6-well plates and incubated at 37 °C, 5%
469 CO_2 for 24 h. Cells were washed in PBS and detached by trypsin incubation. After detachment,
470 trypsin was immediately quenched by the addition of culture medium containing 10% FBS.
471 Cells were fixed in 4% PFA in PBS for 20 min at room temperature and then stained with PE-

472 conjugated anti-human CD276 (1:200, Biolegend #331606) or with the corresponding PE-
473 conjugated isotype control (1:200, Biolegend #400112) antibody for 20 min on ice. Labelled
474 cells were resuspended in 2% FBS in PBS, and signals were acquired using a BD
475 LSRFortessa flow cytometer. Cell fluorescence was analyzed using FlowJO software.

476 **Co-culture model**

477 Before initiating the co-culture between DIVs 14-18, the spheroids were checked under the
478 microscope and only round, compact spheroids were selected for implantation. Spheroids
479 were picked up from the 96-well plate with a 10-µl pipette and carefully implanted by placing
480 them on the cerebellar slice. We used a hand-held digital microscope featuring blue excitation
481 LEDs (AM4115T-GFBW, Dinolite) to check if the spheroid had been implanted on the cerebellar
482 slice. The co-culture was initiated 72h before the start of the perfusion culture and of the
483 imaging assay.

484 **Live-cell imaging**

485 All live-cell imaging assays were performed on a Nikon Ti-2 equipped with a spinning disc X-
486 Light confocal unit as described in detail in the experimental setup section.

487 Tissue health

488 Tissue health under perfusion was assessed using live-cell cleaved Casapse-3/7 (Nucview
489 530, Biotium, Freemont CA, US) and NucBlue (R37605, Thermo Fisher Scientific) to
490 counterstain the nuclei of the tissue slices. We perfused the slices after the start of the
491 perfusion culture, 24 h and 48 h into the perfusion culture with a staining solution containing 2
492 drops/mL NucBlue and 2 µM Caspase-3/7 of BSM. Tissue slices were incubated with the
493 staining solution for 1h, before images were acquired at 20X. To determine the imaging settings
494 for the caspase-dye acquisition, we induced apoptosis in tissue slices cultured on a control-
495 chip through incubation with 2 µM Staurosporine for 24 h. The positive control was
496 subsequently stained with the same staining solution containing 2 drops/mL NucBlue and 2
497 µM Caspase-3/7 and imaging settings were determined. As a real-time, positive control during
498 perfusion culturing, apoptosis was induced by exposing one chip to 40 µM Doxorubicin in BSM
499 and incubation for 2h before imaging. The number of apoptotic cells and the total number of
500 cells per image were estimated using the cell density counting workflow of Ilastik 1.4.0. [57] For
501 each tissue slice and time point, 3 different areas were imaged. Tissue viability was then
502 calculated by the ratio of caspase-positive cells to the total number of cells.

503 Calcium imaging

504 On-chip calcium imaging of the transduced slices was conducted in artificial cerebrospinal fluid
505 (aCSF) and under continuous perfusion to avoid potential clogging of the tubing due to the
506 high salt concentration. The composition of the used aCSF is listed in **Table 1**. All reagents for
507 the aCSF were purchased from Sigma-Aldrich. After image acquisition, the medium was
508 changed back to BSM, and the stop-and-go protocol was resumed. We acquired calcium
509 dynamics in a single plane for 5 min using a 20X (NA 0.45) dry or a 40X (NA 0.8) water
510 immersion objective with an exposure time of 800 ms and 10% resp. 8% laser power.

511 Medulloblastoma co-culture model

512 We used 10X (NA 0.45) dry, 20X dry (NA 0.45) and 40X (NA 0.8) water-immersion objectives
513 to acquire images of tumor cell invasion and tumor-host interactions. Time lapses at 20X and
514 40X with high temporal resolution (every 3 min) were acquired during perfusion stops.
515 Overnight, we acquired images at 10X synchronized to the perfusion stops; the images were
516 taken 17 min and 51 min after the flow had stopped.

517 **Immunocytochemistry**

518 Tissues were fixed for 1h in 4% PFA (28908, Thermo Fisher Scientific), diluted in 1X PBS,
519 either i) on a shaker, for slices that were cultured under static conditions, or ii) under continuous
520 perfusion, for on-chip samples. After fixation, samples were cut out from the insert or the chip
521 and stored in PBS at 4°C until staining. Tissues were permeabilized for 5 min in 0.25% Trypsin-
522 EDTA (25200056, Thermo Fisher Scientific), followed by a 1h blocking step in 1X PBS with 3%
523 FBS, 3% BSA (diluted from A1595, Thermo Fisher Scientific) and 0.3% Triton-X100 (X100,
524 Sigma-Aldrich). Primary antibodies were diluted in PBS with 3% FBS, 3% BSA, and samples
525 were incubated overnight under agitation at 4°C. Samples were then washed thrice for 10 min
526 using PBS with 5% BSA. Secondary antibodies were diluted with DAPI (75004, Stemcell
527 Technologies, Basel, Switzerland) in PBS containing 3% FBS and 3% BSA and incubated at
528 room temperature for 3 h. Next, samples were washed three times 10 min with 1X PBS before
529 mounting on 75 mm x 25 mm glass slides using ProLong Glass antifade mountant (P36984,
530 Thermo Fisher Scientific) medium and covering with a #1 coverslip. Mounted samples were
531 imaged with a Nikon Ti2 spinning-disc confocal using a 10X dry and 40X water-immersion
532 objective.

533 The following primary antibodies were used: rabbit anti-Calbindin (1:1000 dilution, ab108404,
534 abcam), guinea-pig anti-GFAP (1:2000 dilution, 173 308, Synaptic Systems), chicken anti-
535 NeuN (1:500 dilution, ABN91MI, Fisher Scientific), rabbit anti-HIF-1α (1:500 dilution,
536 ab179483, abcam) and rabbit anti-S100β (1:100, ab52642, abcam). As secondary antibodies
537 we used Alexa Fluor donkey anti-rabbit 647 (A21206, Thermo Fisher Scientific), Alexa Fluor
538 donkey anti-chicken 488 (A78952, Thermo Fisher Scientific), and Alexa Fluor goat anti-guinea
539 pig 555 (A21435, Thermo Fisher Scientific) at 1:200 dilution. Hoechst was added to the
540 secondary antibody solution at a dilution of 1:200.

541 **Image Analysis**

542 Tissue integrity

543 Purkinje cell somas were segmented in stacks of 10 µm acquired at 0.4µm z-step size using
544 Imaris v10.0.1 to determine the volume of each Purkinje cell soma and the number of cells per
545 ROI. To normalize the number of cells with respect to the area of the Purkinje cell layer (PCL),
546 we created maximum intensity projections of the ROIs. Next, boundary boxes of the PCL were
547 drawn in ImageJ (2.14/1.54f) using the polygon tool and measured, and the number of
548 segmented cells was divided by the measured PCL area.

549 Hypoxia

550 Positive controls to determine correct imaging settings of hypoxic cerebellar slices were
551 generated by submerging slices cultured on inserts under either 1 mL or 2 mL of medium,
552 mimicking conditions during upright imaging. We used Imaris v10.0.1 to assess hypoxic cells
553 in a 10-µm stack acquired in the middle of the tissue slice. Nuclei were segmented as surfaces,
554 while HIF-1alpha expression was segmented using the spots tool. To determine the number of
555 truly hypoxic cells, the number of HIF-1alpha spots within nuclei surfaces was calculated. The
556 increase of hypoxic cells under the different conditions was then calculated as an x-fold
557 increase in hypoxic cells with respect to the average percentage of hypoxic cells detected in
558 the standard ALI culture on tissue culture inserts. In total, we cultured 8 slices from 2
559 independent experiments under pulsatile flow and analyzed images from 2-3 ROIs per slice.

560 Calcium imaging

561 We used AQuA2 to analyze the calcium dynamics in transduced astrocytes[58]. Preprocessing
562 of the acquired files included the removal of the first 21 frames of each acquisition, since we
563 observed a strong intensity decay within the whole ROI, likely due to activation of Calcium

channels by the laser light[36]. Batch processing of all acquired files was performed using Matlab (R2024a, The Mathworks, Inc., US) after confirming the settings using three to four different acquisitions. The following parameters were used for 40X acquisitions: median filter 1.5, Gaussian filter radius 0.5, intensity threshold 2.8, minimum duration 4, minimum size (px) 15, minimum seed size 0.01, Z score 3.5, maximum dissimilarity 0.7, minimum source size 0.01, sensitivity level 7. For 20X acquisitions the parameters changed to the following: median filter 3, Gaussian filter radius 0.7, intensity threshold 2, minimum duration 5, minimum size (px) 18, minimum seed size 0.01, z score 1.8, maximum dissimilarity 0.7, minimum source size 0.01, sensitivity level 8. After the batch processing, results of detected events were further filtered to include only events with an event size between 10-2500 μm^2 for 40X images and 20-2500 μm^2 for 20X images as well as an event duration between 1.6 and 60 s.

Cell tracking and particle image velocimetry:

Single cells were tracked manually using the Manual Tracking plugin in Fiji's ImageJ (v.1.54f) [59]. By manually clicking on the centroid of a single cell at each time point, this method tracks cell movements along XY coordinates, velocity, and displacement from a series of time-resolved images. The cell trajectories are then visualized using Seaborn and Matplotlib in Python, plotting XY coordinates and displacement over a 12-hour acquisition period.

To estimate cell velocity and displacements of tumoral cells and astrocytes, we analyzed the overnight timelapse images using the PIVLab [60] Matlab app for particle image velocimetry. The acquired series of time-resolved images were pre-processed by subtracting the mean intensity across the image series and then processed using a multipass FFT window deformation method to extract the velocity fields. A four-pass cross-correlation approach was applied, starting with an interrogation area of 312 pixels and a step size of 100 pixels. In each subsequent pass, both the interrogation area and step size were reduced by 50%. The mean and standard deviation of velocity across the 12-hour acquisition period were visualized as a heatmap.

Quantification of B7-H3-mNG localization:

A 10-µm-long line with a width of 100 pixels was drawn across the leading-edge area in the direction of migration or perpendicularly across cell-cell contacts in the B7-H3-mNG fluorescent channel in ImageJ. The lines were centered to the leading edge for lamellipodial B7-H3 or to the cell-cell contacts. The profile of the line was plotted using ImageJ, and the grey values were determined every 0.09 µm. The sum of all grey values was calculated, and the percentage of total grey values calculated every 0.09 µm was plotted. An unpaired t-test with individual variance for each row was performed. The false discovery rate was calculated using a two-stage step-up approach[61].

Data Visualization and Statistical Analysis

Calcium imaging events were visualized using a custom Matlab script to filter events and visualize events according to occurring frequency distributions.

For the remaining figures, GraphPad Prism was used to visualize data and perform statistical analysis. The data are presented as mean +/- s.e.m.. Distributions were first tested for normality, followed by either an unpaired, one-sided t-test or a one-way ANOVA.

606

Table 1: Composition of the used aCSF for Calcium imaging

Reagent	Working concentration
NaCl	126 mM
KCl	3.5 mM
$NaH_2PO_4.H_2O$	1.2 mM
$MgCl_2.6H_2O$	1.3 mM
$CaCl_2.2H_2O$	2 mM
D-Glucose	11 mM
$NaHCO_3$	25 mM

607

608

References

609 1 Baker, B. M. & Chen, C. S. Deconstructing the third dimension – how 3D culture
610 microenvironments alter cellular cues. *Journal of Cell Science* **125**, 3015-3024
611 (2012). https://doi.org:10.1242/jcs.079509

612 2 Jensen, C. & Teng, Y. Is It Time to Start Transitioning From 2D to 3D Cell Culture?
613 *Frontiers in Molecular Biosciences* **7** (2020).
614 https://doi.org:10.3389/fmolb.2020.00033

615 3 Bassett, D. S. & Gazzaniga, M. S. Understanding complexity in the human brain.
616 *Trends in Cognitive Sciences* **15**, 200-209 (2011).
617 https://doi.org:10.1016/j.tics.2011.03.006

618 4 Cajal, S. R. Y., Azoulay, D. L., swanson, N. & Swanson, I. W. (Oxford University
619 Press, 1995).

620 5 Quail, D. F. & Joyce, J. A. The Microenvironmental Landscape of Brain Tumors.
621 *Cancer Cell* **31**, 326-341 (2017). https://doi.org:10.1016/j.ccell.2017.02.009

622 6 Winkler, F. *et al.* Cancer neuroscience: State of the field, emerging directions. *Cell*
623 **186**, 1689-1707 (2023). https://doi.org:10.1016/j.cell.2023.02.002

624 7 Charles, N. A., Holland, E. C., Gilbertson, R., Glass, R. & Kettenmann, H. The brain
625 tumor microenvironment. *Glia* **60**, 502-514 (2012).

626 8 Hanahan, D. & Monje, M. Cancer hallmarks intersect with neuroscience in the tumor
627 microenvironment. *Cancer Cell* **41**, 573-580 (2023).
628 https://doi.org:10.1016/j.ccell.2023.02.012

629 9 Ferreira, L. P., Gaspar, V. M. & Mano, J. F. Design of spherically structured 3D in vitro
630 tumor models -Advances and prospects. *Acta Biomaterialia* **75**, 11-34 (2018).
631 https://doi.org:https://doi.org/10.1016/j.actbio.2018.05.034

632 10 Govindan, S., Batti, L., Osterop, S. F., Stoppini, L. & Roux, A. Mass Generation,
633 Neuron Labeling, and 3D Imaging of Minibrains. *Frontiers in Bioengineering and*
634 *Biotechnology* **8** (2021). https://doi.org:10.3389/fbioe.2020.582650

635 11 Mariappan, A., Goranci-Buzhala, G., Ricci-Vitiani, L., Pallini, R. & Gopalakrishnan, J.
636 Trends and challenges in modeling glioma using 3D human brain organoids. *Cell*
637 *Death & Differentiation* **28**, 15-23 (2021). https://doi.org:10.1038/s41418-020-00679-7

638 12 Birtele, M., Lancaster, M. & Quadrato, G. Modelling human brain development and
639 disease with organoids. *Nature Reviews Molecular Cell Biology* (2024).
640 https://doi.org:10.1038/s41580-024-00804-1

641 13 Qian, X., Song, H. & Ming, G.-l. Brain organoids: advances, applications and
642 challenges. *Development* **146** (2019). https://doi.org:10.1242/dev.166074

643 14 Andrews, M. G. & Kriegstein, A. R. Challenges of Organoid Research. *Annu Rev*
644 *Neurosci* **45**, 23-39 (2022). https://doi.org:10.1146/annurev-neuro-111020-090812

645 15 Bhaduri, A., Andrews, M. G., Kriegstein, A. R. & Nowakowski, T. J. Are Organoids
646 Ready for Prime Time? *Cell Stem Cell* **27**, 361-365 (2020).
647 https://doi.org:https://doi.org/10.1016/j.stem.2020.08.013

648 16 Park, G., Rim, Y. A., Sohn, Y., Nam, Y. & Ju, J. H. Replacing Animal Testing with Stem
649 Cell-Organoids : Advantages and Limitations. *Stem Cell Reviews and Reports* **20**,
650 1375-1386 (2024). https://doi.org:10.1007/s12015-024-10723-5

651 17 Humpel, C. Organotypic brain slice cultures: A review. *Neuroscience* **305**, 86-98
652 (2015). https://doi.org:10.1016/j.neuroscience.2015.07.086

653 18 Croft, C. L., Futch, H. S., Moore, B. D. & Golde, T. E. Organotypic brain slice cultures
654 to model neurodegenerative proteinopathies. *Mol Neurodegener* **14**, 45 (2019).
655 https://doi.org:10.1186/s13024-019-0346-0

656 19 Stoppini, L., Buchs, P. A. & Muller, D. A simple method for organotypic cultures of
657 nervous tissue. *J Neurosci Methods* **37**, 173-182 (1991).
658 https://doi.org:10.1016/0165-0270(91)90128-m

659 20 Eisemann, T. *et al.* An advanced glioma cell invasion assay based on organotypic
660 brain slice cultures. *BMC Cancer* **18**, 103 (2018). https://doi.org:10.1186/s12885-018-
661 4007-4

662 21 Santhana Kumar, K. *et al.* TGF-β Determines the Pro-migratory Potential of bFGF
663 Signaling in Medulloblastoma. *Cell Reports* **23**, 3798-3812.e3798 (2018).
664 https://doi.org:https://doi.org/10.1016/j.celrep.2018.05.083

665 22 Steindl, A. & Valiente, M. Potential of ex vivo organotypic slice cultures in neuro-
666 oncology. *Neuro-Oncology* (2024). https://doi.org:10.1093/neuonc/noae195

667 23 Parker, J. J., Lizarraga, M., Waziri, A. & Foshay, K. M. A Human Glioblastoma
668 Organotypic Slice Culture Model for Study of Tumor Cell Migration and Patient-
669 specific Effects of Anti-Invasive Drugs. *J Vis Exp* (2017).
670 https://doi.org:10.3791/53557

671 24 Pan, Y. *et al.* NF1 mutation drives neuronal activity-dependent initiation of optic
672 glioma. *Nature* **594**, 277-282 (2021). https://doi.org:10.1038/s41586-021-03580-6

673 25 Liu, Y. *et al.* Astrocytes Promote Medulloblastoma Progression through Hedgehog
674 Secretion. *Cancer Research* **77**, 6692-6703 (2017). https://doi.org:10.1158/0008-
675 5472.Can-17-1463

676 26 Chen, Q. *et al.* Carcinoma–astrocyte gap junctions promote brain metastasis by
677 cGAMP transfer. *Nature* **533**, 493-498 (2016). https://doi.org:10.1038/nature18268

678 27 Misra, S. *et al.* Ex vivo organotypic culture system of precision-cut slices of human
679 pancreatic ductal adenocarcinoma. *Sci Rep* **9**, 2133 (2019).
680 https://doi.org:10.1038/s41598-019-38603-w

681 28 Migliavacca, J., Züllig, B., Capdeville, C., Grotzer, M. A. & Baumgartner, M.
682 Cooperation of Striatin 3 and MAP4K4 promotes growth and tissue invasion.
683 *Communications Biology* **5**, 795 (2022). https://doi.org:10.1038/s42003-022-03708-y

684 29 Mann, B. *et al.* A living ex vivo platform for functional, personalized brain cancer
685 diagnosis. *Cell Reports Medicine* **4**, 101042 (2023).
686 https://doi.org:https://doi.org/10.1016/j.xcrm.2023.101042

687 30 Minami, N. *et al.* Organotypic brain explant culture as a drug evaluation system for
688 malignant brain tumors. *Cancer Medicine* **6**, 2635-2645 (2017).
689 https://doi.org:https://doi.org/10.1002/cam4.1174

690 31 Gries, A. *et al.* Aurora kinase B is required for growth and expansion of
691 medulloblastoma cells in the tissue context. *Neoplasia* **59**, 101078 (2025).
692 https://doi.org:https://doi.org/10.1016/j.neo.2024.101078

693 32 Gahwiler, B. H. Organotypic monolayer cultures of nervous tissue. *J Neurosci*
694 *Methods* **4**, 329-342 (1981). https://doi.org:10.1016/0165-0270(81)90003-0

695 33 Northcott, P. A. *et al.* Medulloblastoma. *Nat Rev Dis Primers* **5**, 11 (2019).
696 https://doi.org:10.1038/s41572-019-0063-6

697 34 Neve, A., Santhana Kumar, K., Tripolitsioti, D., Grotzer, M. A. & Baumgartner, M.
698 Investigation of brain tissue infiltration by medulloblastoma cells in an ex vivo model.
699 *Sci Rep* **7**, 5297 (2017). https://doi.org:10.1038/s41598-017-05573-w

700 35 Keller, D., Erö, C. & Markram, H. Cell Densities in the Mouse Brain: A Systematic
701 Review. *Frontiers in Neuroanatomy* **12** (2018).
702 https://doi.org:10.3389/fnana.2018.00083

703 36 Semyanov, A., Henneberger, C. & Agarwal, A. Making sense of astrocytic calcium
704 signals — from acquisition to interpretation. *Nature Reviews Neuroscience* **21**, 551-
705 564 (2020). https://doi.org:10.1038/s41583-020-0361-8

706 37 Bazargani, N. & Attwell, D. Astrocyte calcium signaling: the third wave. *Nature*
707 *Neuroscience* **19**, 182-189 (2016). https://doi.org:10.1038/nn.4201

708 38 Venkataramani, V. *et al.* Glioblastoma hijacks neuronal mechanisms for brain
709 invasion. *Cell* **185**, 2899-2917.e2831 (2022).
710 https://doi.org:https://doi.org/10.1016/j.cell.2022.06.054

711 39 Duarte, T. T., Teixeira, S. A., Gonzalez-Reyes, L. & Reis, R. M. Decoding the Roles of
712 Astrocytes and Hedgehog Signaling in Medulloblastoma. *Current Oncology* **28**, 3058-
713 3070 (2021).

714 40 Mi, X. *et al.* Fast, Accurate, and Versatile Data Analysis Platform for the Quantification
715 of Molecular Spatiotemporal Signals. *bioRxiv*, 2024.2005.2002.592259 (2024).
716 https://doi.org:10.1101/2024.05.02.592259

717 41 Farmer, W. T. *et al.* Neurons diversify astrocytes in the adult brain through sonic
718 hedgehog signaling. *Science* **351**, 849-854 (2016).
719 https://doi.org:doi:10.1126/science.aab3103

720 42 Hoogland, T. M. & Kuhn, B. Recent Developments in the Understanding of Astrocyte
721 Function in the Cerebellum In Vivo. *The Cerebellum* **9**, 264-271 (2010).
722 https://doi.org:10.1007/s12311-009-0139-z

723 43 Pinto, G., Brou, C. & Zurzolo, C. Tunneling Nanotubes: The Fuel of Tumor
724 Progression? *Trends in Cancer* **6**, 874-888 (2020).
725 https://doi.org:https://doi.org/10.1016/j.trecan.2020.04.012

726 44 Venkataramani, V. *et al.* Disconnecting multicellular networks in brain tumours. *Nature*
727 *Reviews Cancer* **22**, 481-491 (2022). https://doi.org:10.1038/s41568-022-00475-0

728 45 Vilchez Mercedes, S. A. *et al.* Decoding leader cells in collective cancer invasion.
729 *Nature Reviews Cancer* **21**, 592-604 (2021). https://doi.org:10.1038/s41568-021-
730 00376-8

731 46 Mayor, R. & Etienne-Manneville, S. The front and rear of collective cell migration.
732 *Nature Reviews Molecular Cell Biology* **17**, 97-109 (2016).
733 https://doi.org:10.1038/nrm.2015.14

734 47 Haydar, D. *et al.* Cell-surface antigen profiling of pediatric brain tumors: B7-H3 is
735 consistently expressed and can be targeted via local or systemic CAR T-cell delivery.
736 *Neuro Oncol* **23**, 999-1011 (2021). https://doi.org:10.1093/neuonc/noaa278

737 48 Epperly, R., Gottschalk, S. & DeRenzo, C. CAR T cells redirected to B7-H3 for
738 pediatric solid tumors: Current status and future perspectives. *EJC Paediatr Oncol* **3**
739 (2024). https://doi.org:10.1016/j.ejcped.2024.100160

740 49 Toepke, M. W. & Beebe, D. J. PDMS absorption of small molecules and
741 consequences in microfluidic applications. *Lab on a Chip* **6**, 1484-1486 (2006).
742 https://doi.org:10.1039/B612140C

743 50 Kats, I. *et al.* Spatio-temporal transcriptomics of chromothriptic SHH-medulloblastoma
744 identifies multiple genetic clones that resist treatment and drive relapse. *Nature*
745 *Communications* **15**, 10370 (2024). https://doi.org:10.1038/s41467-024-54709-w

746 51 Zhao, B. *et al.* Immune checkpoint of B7-H3 in cancer: from immunology to clinical
747 immunotherapy. *J Hematol Oncol* **15**, 153 (2022). https://doi.org:10.1186/s13045-022-
748 01364-7

749 52 Schönholzer, M. T. *et al.* Real-time sensing of MAPK signaling in medulloblastoma
750 cells reveals cellular evasion mechanism counteracting dasatinib blockade of ERK
751 activation during invasion. *Neoplasia* **22**, 470-483 (2020).
752 https://doi.org:https://doi.org/10.1016/j.neo.2020.07.006

753 53 Lohasz, C. *et al.* A Microphysiological Cell-Culturing System for Pharmacokinetic
754 Drug Exposure and High-Resolution Imaging of Arrays of 3D Microtissues. *Frontiers*
755 *in Pharmacology* **12** (2021). https://doi.org:10.3389/fphar.2021.785851

756 54 Falsig, J. & Aguzzi, A. The prion organotypic slice culture assay—POSCA. *Nature*
757 *Protocols* **3**, 555-562 (2008). https://doi.org:10.1038/nprot.2008.13

758 55 Roper, S. J., Linke, F., Scotting, P. J. & Coyle, B. 3D spheroid models of paediatric
759 SHH medulloblastoma mimic tumour biology, drug response and metastatic
760 dissemination. *Scientific Reports* **11**, 4259 (2021). https://doi.org:10.1038/s41598-
761 021-83809-6

762 56 Riedl, J. *et al.* Lifeact: a versatile marker to visualize F-actin. *Nat Methods* **5**, 605-607
763 (2008). https://doi.org:10.1038/nmeth.1220

764 57 Berg, S. *et al.* ilastik: interactive machine learning for (bio)image analysis. *Nature*
765 *Methods* **16**, 1226-1232 (2019). https://doi.org:10.1038/s41592-019-0582-9

766 58 Wang, Y. *et al.* Accurate quantification of astrocyte and neurotransmitter fluorescence
767 dynamics for single-cell and population-level physiology. *Nature Neuroscience* **22**,
768 1936-1944 (2019). https://doi.org:10.1038/s41593-019-0492-2

769 59 Cordelières, F. P. *Manual Tracking*, <https://imagej.net/ij/plugins/track/track.html>
770 (2005).

771 60 Thielicke, W. & Sonntag, R. Particle Image Velocimetry for MATLAB: Accuracy and
772 enhanced algorithms in PIVlab. (2021).

61 Benjamini, Y., Krieger, A. M. & Yekutieli, D. Adaptive linear step-up procedures that control the false discovery rate. *Biometrika* **93**, 491-507 (2006).